Processing and characterization of a multibeam sputtered nanocrystalline CoCrFeNi multi-principle element alloy film

MSc thesis written by

Péter Nagy[a,b]

Supervisor:

Jenő Gubicza[a]

External Supervisor:

László Pethö[b]

[a]Department of Materials Physics, Eötvös Loránd University, Budapest, Hungary

[b]EMPA Swiss Federal Laboratories for Materials Science and Technology, Laboratory for Mechanics of Materials and Nanostructures, Feuerwerkerstrasse 39, Thun CH-3602, Switzerland

Department of Materials Physics, Eötvös Loránd University, Budapest, Hungary

2020

Table of Contents

1. Motivation 4
2. Introduction 4
3. Theoretical overview 6
3.1. High Entropy alloys (HEAs) 6
3.1.1. Thermodynamics of HEAs 6
3.1.2. Cocktail effect 7
3.1.3. High-entropy effect 8
3.1.4. Lattice distortion 10
3.1.5. Sluggish diffusion effect 10
3.1.6. High entropy alloy thin films 11
3.2. Physical vapor deposition (PVD) 13
3.2.1. Introduction 13
3.2.2. Comparison of different type of PVD techniques 14
3.3. Electron cyclotron resonance 16
4. Material and methods 17
4.1. The sputtering system 17
4.2. The ion source 19
4.3. Analysis of the chemical composition and the film thickness 21
4.4. Investigation of the microstructure 23
4.4.1. X-ray diffraction line profile analysis (XLPA) 23
4.4.2. Transmission electron microscopy (TEM) 25
4.4.3. Pole figure measurement 26
4.5. Nanoindentation 27
5. Results and discussion 30
5.1. The spatial distribution of the film thickness and the chemical composition 30
5.2. Crystallite size and texture of the equimolar CoCrFeNi film 33
5.3. Study of the microstructure by TEM 35
5.4. Comparison of the nanohardness obtained for PVD- and HPT-processed CoCrFeNi MPEAs 38
6. Conclusions 42

7. The contributions of the author 43
8. Outlook 43
Acknowledgment 46
References 47

1. Motivation

Physical vapor deposition (PVD) is a well-known route for manufacturing hard coatings. In recent years, PVD has also been applied to create high-entropy alloy (HEA) thin films. HEAs are multicomponent alloys containing at least five different elements with nearly equal atomic fractions. The alloys containing less elements with similar fractions are called as multi-principle element alloys (MPEAs). To achieve the desired composition, typically, alloy targets are used in the deposition process. The present work demonstrates that MPEA thin films can also be processed using a multiple beam sputtering system in PVD, which does not require preliminary manufacturing of MPEA targets, but rather uses commercially pure metal targets. The effectivity of this technique was demonstrated on a nanocrystalline CoCrNiFe MPEA film with a thickness of about 1 micron. A part of the compositional gradient sample exhibited equal elemental fractions. The microstructure and the hardness of this part of the PVD film were studied in detail, and the results were compared with those obtained on a bulk nanocrystalline sample having the same chemical composition but were prepared by the high pressure torsion (HPT) technique. The crystallite size and the texture were characterized by X-ray diffraction, while the hardness was measured by nanoindentation. The PVD film exhibited an exceptionally high hardness of 9.8 ± 0.3 GPa, a value that was notably higher than that determined for the HPT sample (7.3 ± 0.3 GPa). This study also demonstrated the capability of this new multiple beam sputtering technique for the production of compositional gradient samples with a wide range of elemental concentrations, enabling combinatorial analysis of MPEAs.

2. Introduction

HEAs exemplify a recent development in materials science [1,2]. HEAs are intensively studied materials due to their impressive mechanical properties, such as very high strength even at high temperatures [3]. The synthesis of HEA materials exploits many different methods such as melt spinning [2], electromagnetic stirring [4], vacuum arc melting [5], or mechanical alloying [6]. In addition, severe plastic deformation (SPD) through high pressure torsion (HPT) technique was also applied on different HEA materials in order to obtain nanocrystalline microstructures [7-10].

The effect of the chemical composition on the structure and properties of HEA films can be studied on combinatorial samples. Recently, Marshal et al. reported the synthesis of a combinatorial HEA thin film by sputtering [11]. Formerly, PVD techniques developed for producing HEA layers used alloy targets in the deposition process.

There are two definitions of HEAs. The first is the composition-based definition which says that HEAs contain at least five elements with the atomic concentrations between 5 and 35%. The second is the entropy-based definition which calls a material as HEA if the configuration entropy is higher than $1.61R$, where R is the universal gas constant $\left(8.314 \frac{J}{K*mol}\right)$. The composition-based definition allows to call materials as HEA with configuration entropy smaller than $1.61R$. For instance, for a composition 5% A, 5% B, 20% C, 35% D and 35% E (A, B, C, D and E are the constituents of the alloy), the configuration entropy is only $1.36R$. Therefore, sometimes the four-component equimolar alloys are also called as HEAs since their configuration entropy is higher than this value (namely $1.39R$). However, the name of HEAs indicates that the alloy must have a high entropy, therefore as a compromise it is suggested that a HEA must have a higher configuration entropy than $1.5R$. Therefore, the equimolar materials with four components can not be called as HEAs but rather they are referred to as Multi-Principal Element Alloy (MPEA) in the literature. This terminology will also be used for the material studied in this thesis.

In this work, we aim to introduce a novel PVD method, which is suitable to create combinatorial MPEA samples. Namely, a MPEA thin film with the composition of CoCrFeNi is produced using a multiple beam sputtering (MBS) system in PVD, which does not require preliminary manufacturing of MPEA targets, but rather uses commercially pure metal targets. The spatial distribution of the thickness and the chemical composition of the nanocrystalline CoCrFeNi thin film processed by MBS were also investigated. The grain and crystallite sizes as well as the texture for the equimolar CoCrFeNi composition were studied in detail. The results were compared with those obtained on a bulk nanocrystalline sample with the same chemical composition but processed by HPT.

3. Theoretical overview

3.1. High Entropy alloys (HEAs)

3.1.1. Thermodynamics of HEAs

HEAs are alloys that contain multiple elements with equal or nearly equal molar ration. In the case of conventional alloys, we usually have one main element and a small addition of supplementary elements. The properties of these components could be understood through the investigation of Gibbs free energy (*G*). According to the law of thermodynamics, the Gibbs free energy is minimal in a system when it is in equilibrium. In case of an alloy, the mixing component of Gibbs free energy will be relevant, which could be expressed as:

$$\Delta G_{mix} = \Delta H_{mix} - T\Delta S_{mix}, \quad (1)$$

where ΔG_{mix} is the Gibbs free energy of mixing, ΔH_{mix} is the enthalpy of mixing, T is the temperature in Kelvin, and ΔS_{mix} is the entropy of mixing. In equation (1), the term $T\Delta S_{mix}$ is becoming more significant at a higher temperature. If we keep the mixing enthalpy constant, we can see that the Gibbs free energy will be lower as the mixing entropy increases, and it will lead to a more stable system. The configuration entropy in a macrostate is related to the number of possible microstates. The relation between the entropy and the possible microstates could be expressed as:

$$S = k * ln(W), \quad (2)$$

where k is the Boltzmann's constant $\left(1.38 * 10^{-23}\frac{J}{K}\right)$ and W is the number of possible microstates. For a solid solution with *N* components, the mixing entropy is the following:

$$\Delta S_{mix} = -R\sum_i c_i ln\, c_i. \quad (3)$$

For equimolar compositions, equation (3) can be simplified as:

$$\Delta S_{mix} = -R * N * \left(\frac{1}{N} ln \frac{1}{N}\right) = RlnN. \quad (4)$$

For conventional metallic alloys, their fusion entropy (increase in entropy when melting) is usually ~$1R$ [12]. In the case of an equimolar alloy with three components, the value of ΔS_{mix} is $1.1R$. This is usually higher than their fusion entropy, and the difference between them increases further as we increase the numbers of components. There are four "core effects" which are often used to describe HEAs; they are the "cocktail" effect, the high-entropy effect, the lattice distortion effect, and the sluggish diffusion [13].

3.1.2. Cocktail effect

The mechanical properties of HEA materials usually differ from the properties of their component materials [14]. This is the "cocktail effect" which means we could not predict the properties of the HEAs from the properties of their components. The reason behind this effect is that the properties not only depends on the alloying materials but also their interaction with each other. This effect was firstly described by Ranganathan [15]. In the case of traditional alloys, the mechanical properties are usually determined by one dominant component of the alloying materials. As you can see in Figure 1, the different basic alloys have a well defined Young's modulus. For example, for all aluminum-based alloys the Young's modulus is around 75 GPa. On the other hand, the HEA materials shown in this figure have a wide range of Young's modulus.

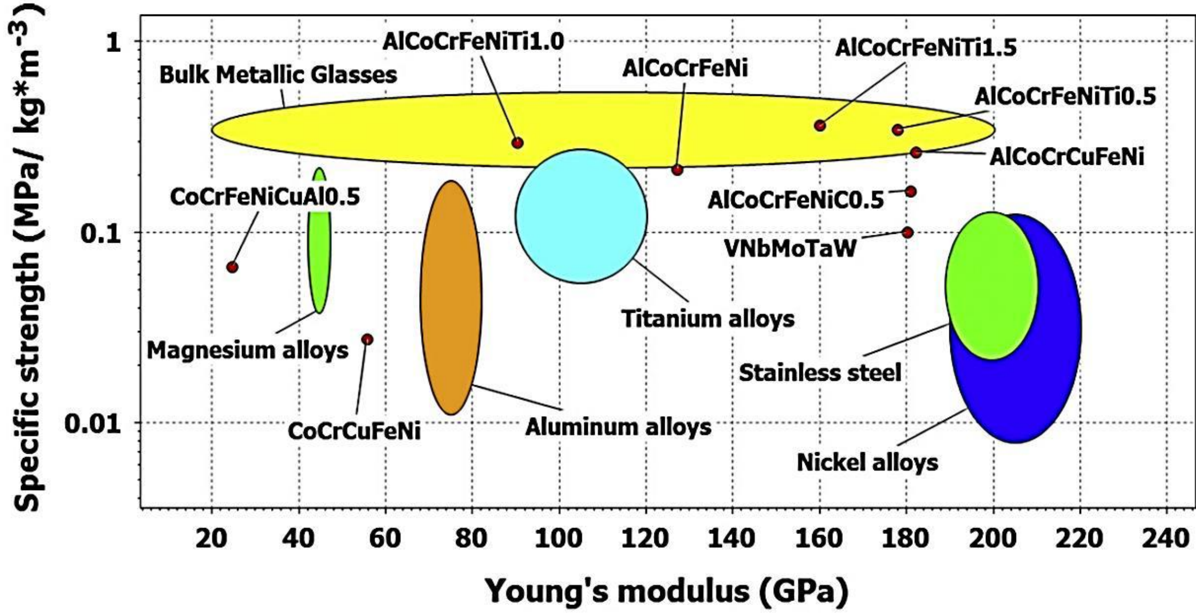

Figure 1. Specific yield strength vs. Young's modulus for different alloys including HEAs. HEAs are compared with other materials, such as bulk metallic glasses and structural alloys [16].

3.1.3. High-entropy effect

In the cases of HEAs, it was obtained that they rather form solid solutions instead of intermetallic compounds due to the high mixing entropy [1,2,17], especially at high temperatures, because the entropy contribution in the Gibbs free energy increases with the temperature as shown in equation (1). It does not mean that every alloy having multiple components with equal fractions form a solid solution. It was found that only specific compositions behave this way [18]. The high entropy effect blocks the formation of intermetallic states and helps the formation of a solid solution. The enthalpy in solid solution is not enough to stabilize the system, and the mixing enthalpy should also be considered [17]:

$$\Delta H_{mix} = \sum_{i=1,i\neq j}^{N} 4\Delta H_{ij}^{mix} c_i c_j, \quad (5)$$

where c_i and c_j are the atomic concentrations of the ith and jth elements, respectively, ΔH_{ij}^{mix} is the enthalpy of mixing between the ith and jth elements at the equimolar composition. According to Zhang et al. [19], ΔH_{mix} should be between -10 and 5 kJ/mol to form a complete solid solution. The mixing entropy and the mixing enthalpy could be combined into a single variable:

$$\Omega = \frac{T_m \, \Delta \, S_{mix}}{|\Delta H_{mix}|} \, , \tag{6}$$

where Tm is the average melting point of the elements in the alloy. Ω is a unitless parameter and should be ≥1.1 to form a solid solution in HEA materials. Figure 2 shows a schematic illustration of the mixing of the constituents.

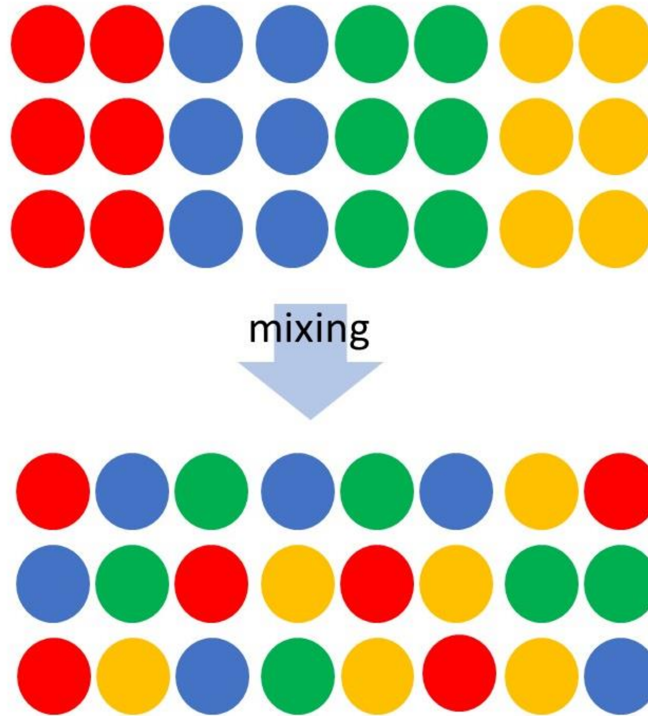

Figure 2. Schematic illustration of a four-component alloy before and after mixing of the constituents.

3.1.4. *Lattice distortion*

The lattice distortion can influence the properties of HEAs. The reason behind this distortion is the different radii of and bonding energies of the component [20,21]. The lattice distortion in HEA materials has a significant effect on mechanical properties. The large friction stress during dislocation glide in the severely distorted lattice increases the strength and the hardness of HEAs [18]. A schematic illustration of this effect is shown in Figure 3.

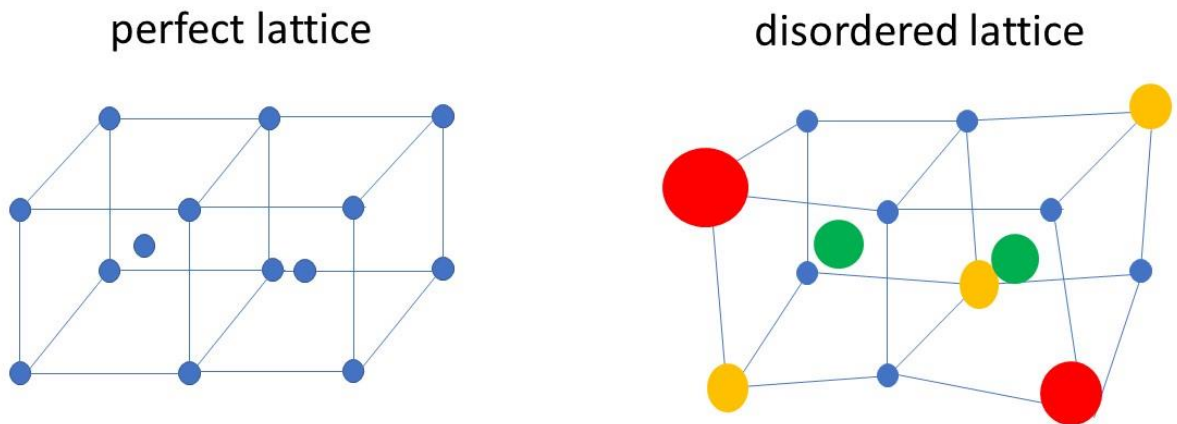

Figure 3. Schematic illustration of a perfect and a disordered lattice.

3.1.5. Sluggish diffusion effect

Diffusion-driven phase transformation requires the simultaneous diffusion of different atoms for the formation of new phases. It was suggested that in the case of HEA materials, the diffusion and phase transformation kinetics are slower than in conventional alloys [22]. In case of disordered solid solutions, the neighbors of atoms that move into a vacancy change chemically with its position. The different environment leads to different local potential energy levels. When an atom moves to a lower energy position, it is trapped, which inhibits further diffusion of this atom. [22]. This effect is called as sluggish diffusion.

3.1.6. High entropy alloy thin films

In the last few years, some works reported the successful synthesis of HEA thin films by physical vapor deposition (PVD) [23-25]. Deposition of HEA thin films have already been demonstrated by different PVD methods in the literature. For instance, Gao et al. manufactured a CoCrFeNiAl HEA film via radio frequency (RF) magnetron sputtering PVD [23]. In another case, Nadutov et al. used cathodic arc evaporation (CEA) PVD to deposit AlFeCoNiCuCr HEA [24]. Tsau et al. investigated the electrical resistance of HEA oxide thin films which were produced by oxidation of PVD HEA films [25]. The compositions of these HEA deposits were TiFeCoNiCu, TiFeCoNi and AlCrFeCoNiCu, where all targets were prepared by arc melting, and then vaporized by direct current (DC) PVD. In the work of Gao et al, the authors showed that HEA thin film samples had outstanding mechanical properties such as the high Young's modulus, and the hardness of the film was larger than the value measured on its bulk counterpart [23]. Moreover, the corrosion resistance of this PVD-processed HEA film was better than that for 304 stainless steel in a 3.5 wt% NaCl solution at room temperature [23] as shown in Figure 4.

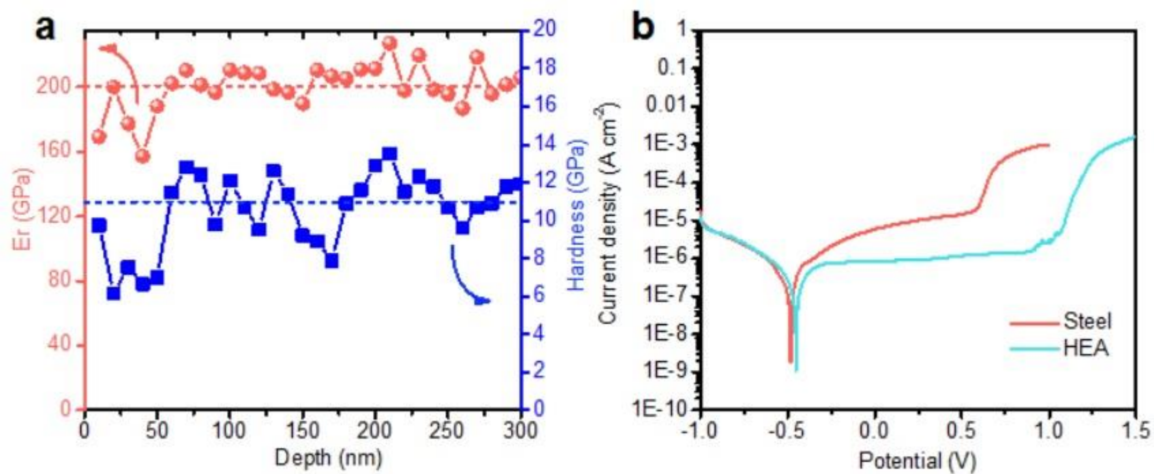

Figure 4. The results of (a) mechanical and (b) corrosion tests for the CoCrFeNiAl HEA film and steel in 3.5 wt % NaCl solution [23].

In the work of Nadutov et al. they investigated an AlFeCoCuCr HEA in as-cast state and as thin coating on cooper and stainless steel substrates. These materials were investigated by X-ray diffraction and Mössbauer spectroscopy. The X-ray diffraction identified two fcc phases and one bcc phase in the as-cast HEA and in both thin films. The Mössbauer spectroscopy revealed two components which belong to a paramagnetic phase and a ferromagnetic phase (see Figure 5). The physical vapor deposition by cathode arc evaporation technology ensures paramagnetic state and better homogeneity of the phases in HEA coating deposited on Cu substrate [24].

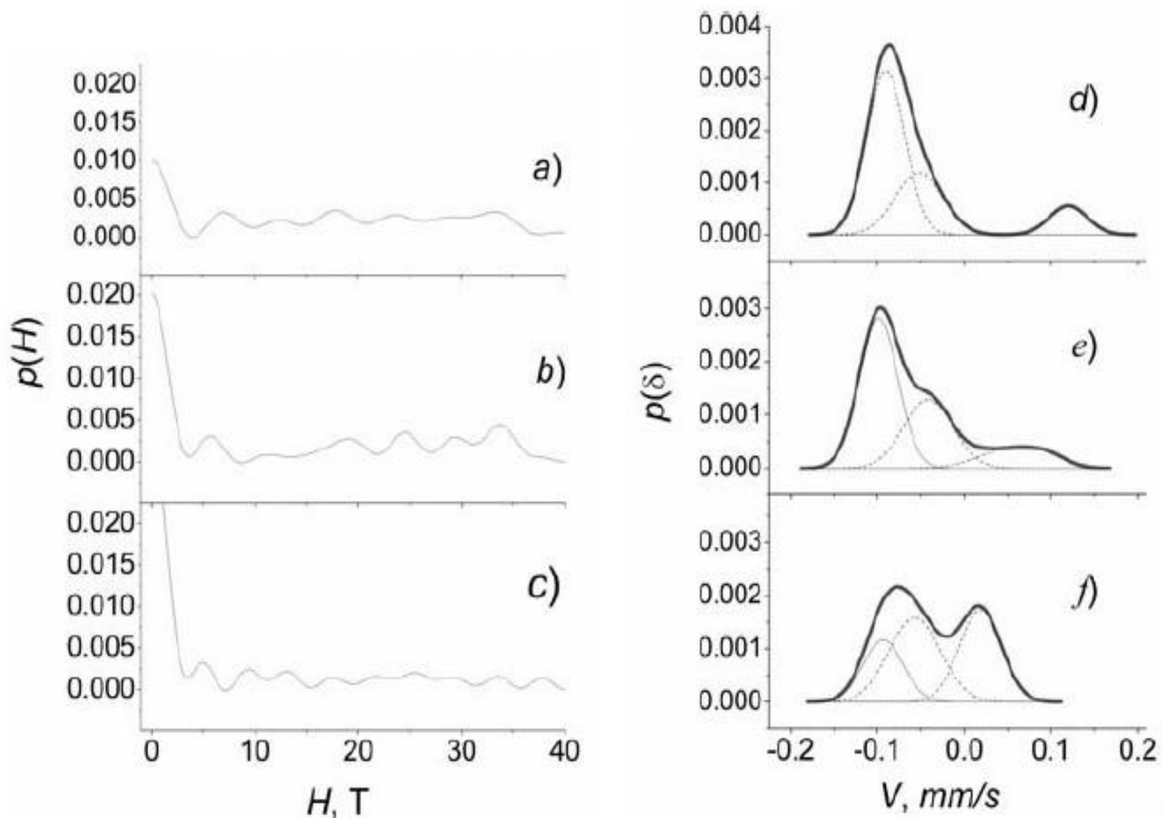

Figure 5. The distribution of hyperfine magnetic fields p(H) (a, b, c) and of the isomer shifts p(H) (d, e, f) in the as-cast AlFeNiCuCr HEA (a, d) and the PVD HEA coating deposited on stainless steel (b, d) and on Cu (c, f) substrates [24].

Tsau et al. investigated the electrical resistivity of HEA thin films. The resistivity of $FeCoNiO_x$, $CrFeCoNiO_x$, $AlFeCoNiO_x$ and $TiFeCoNiO_x$ (named as FCNO, CFCNO, AFCNO, and TFCNO, respectively) were investigated after annealing at different temperatures for different durations.

The room temperature resistivity was close to the values obtained for most metallic alloys. The addition of chromium had no benefit in these systems. Addition of titanium and aluminium could increase their oxidation resistance, and their resistivity kept at lower values after annealing at high temperatures for long periods [25] as it shown in Figure 6. Due to these impressive properties, HEA thin films processed by PVD are promising materials in many applications.

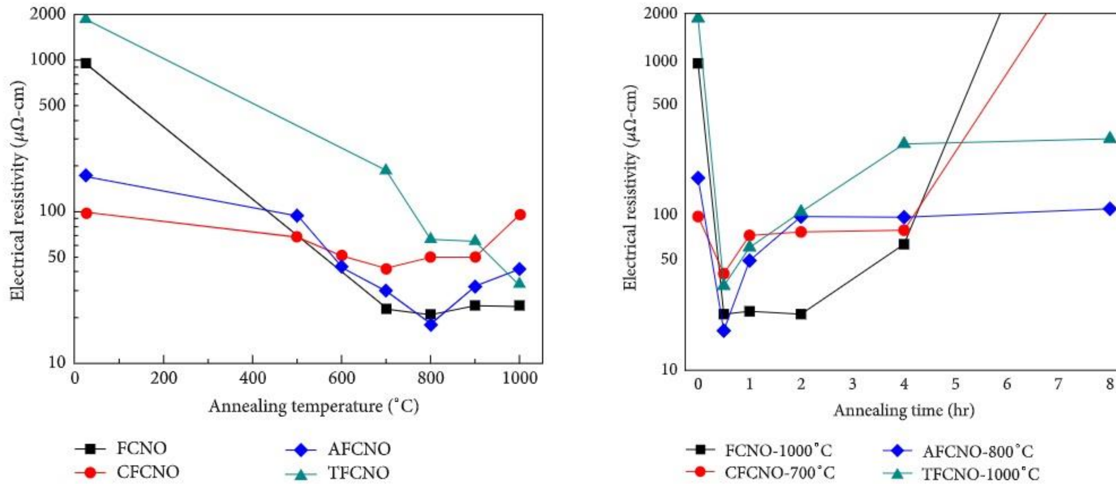

Figure 6. Electrical resistivity of the thin films as a function of annealing temperature and annealing time [25].

3.2. Physical vapor deposition (PVD)

3.2.1. Introduction

PVD is a well-known method to produce thin films and coatings. During this process, atoms or molecules are deposited onto a surface from a solid or liquid source in a vacuum. Usually, the thickness of PVD thin films is between a few nanometers and a few micrometers. Many industrial sectors and research fields apply versatile PVD techniques. Numerous PVD methods have been developed, such as inductively coupled plasma magnetron sputtering (ICP-MS), high power impulse magnetron sputtering (HIPIMS), self-sustained sputtering (SSS), and the hollow

cathode magnetron (HCM) sputtering discharges. For a detailed review, see [26] and the references therein.

3.2.2. Comparison of different type of PVD techniques

The main categories of PVD are ion plating, vapor deposition, arc deposition, vacuum deposition, and sputtering deposition. In the latter method, the deposited particles are vaporized from a surface ("target") by a physical sputtering process. Physical sputtering is a non-thermal vaporization process where the surface atoms are physically ejected from a solid surface by momentum transfer from atomic-sized energetic bombarding particles, which are usually gaseous ions accelerated from a plasma [27]. Figure 7 shows a visual summary of the PVD techniques.

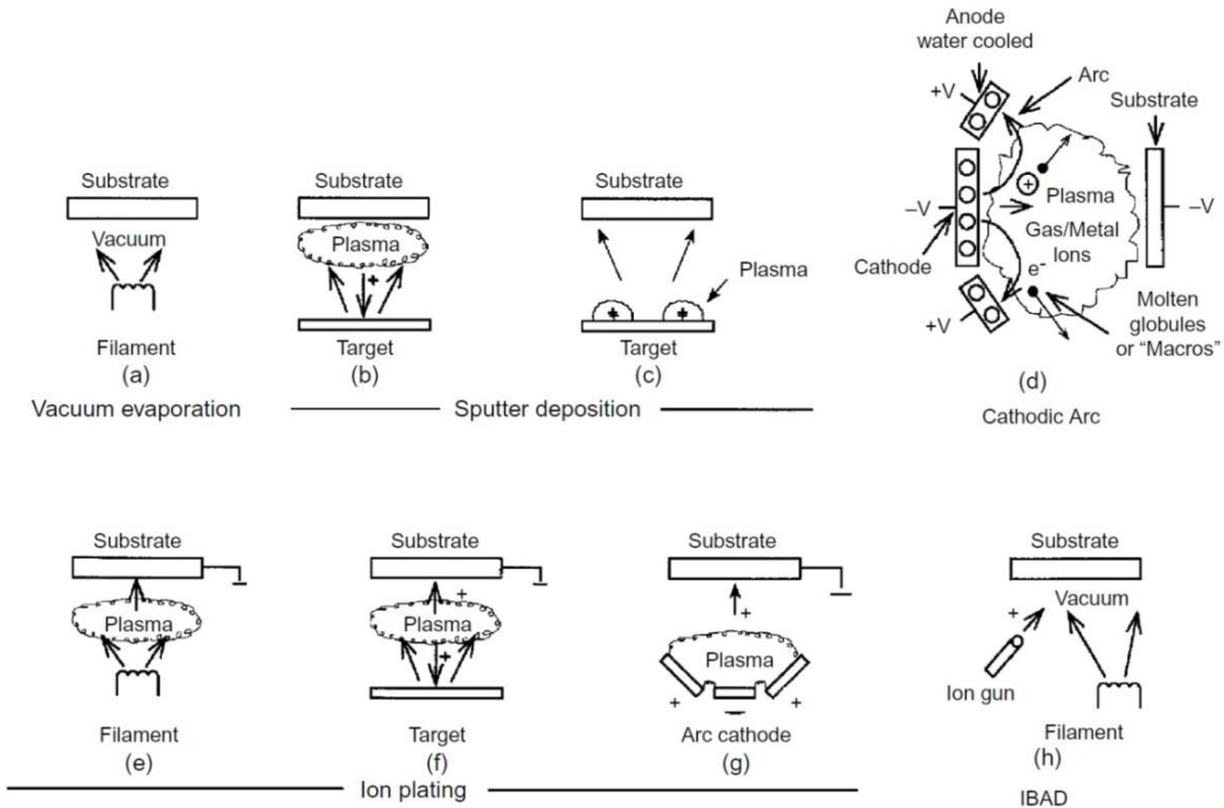

Figure 7. PVD Processing Techniques: (a) Vacuum Evaporation, (b) and (c) Sputter Deposition in a Plasma Environment, (d) Sputter Deposition in a vacuum, (e) Ion Plating in a Plasma Environment with a Thermal Evaporation Source, (f) Ion Plating with a Sputtering Source, (g) Ion Plating with an arc Vaporization Source, and (h) Ion Beam-Assisted Deposition (IBAD) with a Thermal Evaporation Source and Ion Bombardment from an Ion Gun [27].

3.2.2.1. Vacuum evaporation

Vacuum evaporation is a PVD process in which material from a thermal vaporization source reaches the substrate with little or no collision with gas molecules in the space between the source and substrate. The trajectory of the vaporized material is “line of sight.” [27]. Thermal evaporation is generally done by using thermally heated sources such as tungsten wire coils or by high energy electron beam (e-beam) heating of the source material itself [27]. There is no limitation in the quality of the vacuum that can be applied. The higher the vacuum, the lower the gaseous contamination, and the number of collisions. The process can be run in an ultra-high vacuum ($< 10^{-9}\ mbar$). The evaporated particles are not thermalized, and the temperature of the atoms is very high compared to magnetron sputtering.

3.2.2.2. Sputter deposition

Sputter deposition is the deposition of particles vaporized from a surface (“target”) by a physical sputtering process. Physical sputtering is a non-thermal vaporization technique where surface atoms are physically ejected from a solid surface by momentum transfer from an atomic-sized energetic bombarding particle, which is usually a gaseous ion, accelerated from plasma [27]. The process pressure is typically in the range of 10^{-4}-10^{-1}mbar. The relatively low vacuum can eventuate a higher rate of gas contamination in films, but the plasma gas is normally an extremely high purity (usually noble gas) gas like Ar. The target-substrate distance can be from a few cm up to the scale of a meter, and the plasma may fill the whole distance depending on the applied voltage and gas pressure. Compound materials like TiN or TiO_2 can be deposited with the addition of a second, reactive gas, such as N or O_2. The target material can be elemental, alloy, mixture, or a compound (like TiN and TiO_2). The thermalization of the sputtered atoms depends on the applied pressure during the process. The fact that this is not a thermal process has to be highlighted, as it is especially important in amorphous film deposition. High thermalization can help the mechanism of glass formation by giving enough time for the arriving atoms to find the lowest energy position in the random structure. [27]

3.2.2.3. Arc Vapor Deposition

Arc vapor deposition uses a high current, low voltage arc to vaporize a cathodic electrode (cathodic arc) or anodic electrode (anodic arc) and deposit the vaporized material onto the substrate. The vaporized material is highly ionized, and usually, the substrate is biased to accelerate the ions ("film ions") to the substrate surface [27].

3.2.2.4. Ion Plating

Ion plating, which is sometimes called ion-assisted deposition (IAD) or ion vapor deposition (IVD), utilizes concurrent or periodic bombardment of the depositing film by atomic-sized energetic particles to modify and control the properties of the depositing film. In ion plating, the energy, flux, and mass of the bombarding species along with the ratio of bombarding particles to depositing particles are important processing variables. The depositing material may be vaporized either by evaporation, sputtering, arc erosion, or by decomposition of a chemical vapor precursor [27].

3.3. Electron cyclotron resonance

In this work, we utilized a technique called Multi Beam Sputtering, which relies on the use of independent ion sources. These sources work on the principle of electron cyclotron resonance. Electron cyclotron resonance happens when the frequency of incident radiation coincides with the natural frequency of rotation of electron in magnetic fields. Free electrons circle around the magnetic field lines due to the Lorentz force, with frequency

$$f = \frac{e * B}{2\pi\, m_e} (Hz), \tag{7}$$

where B is the magnetic flux density, e the electron charge, and m_e the electron mass. A nonzero velocity component parallel to the magnetic field will cause an electron to spiral along the field lines with a helical path. A nonzero velocity component in a different direction will result in a cycloidal type of path with a net drift perpendicular to the magnetic field. When sending in the microwave, we add an alternating electromagnetic field perpendicular to the magnetic field. In the special case, when the microwave frequency exactly matches the angular frequency of the electrons, the free electrons are continuously accelerated because they change direction in phase with the alternating electric field.

4. Material and methods

4.1. The sputtering system

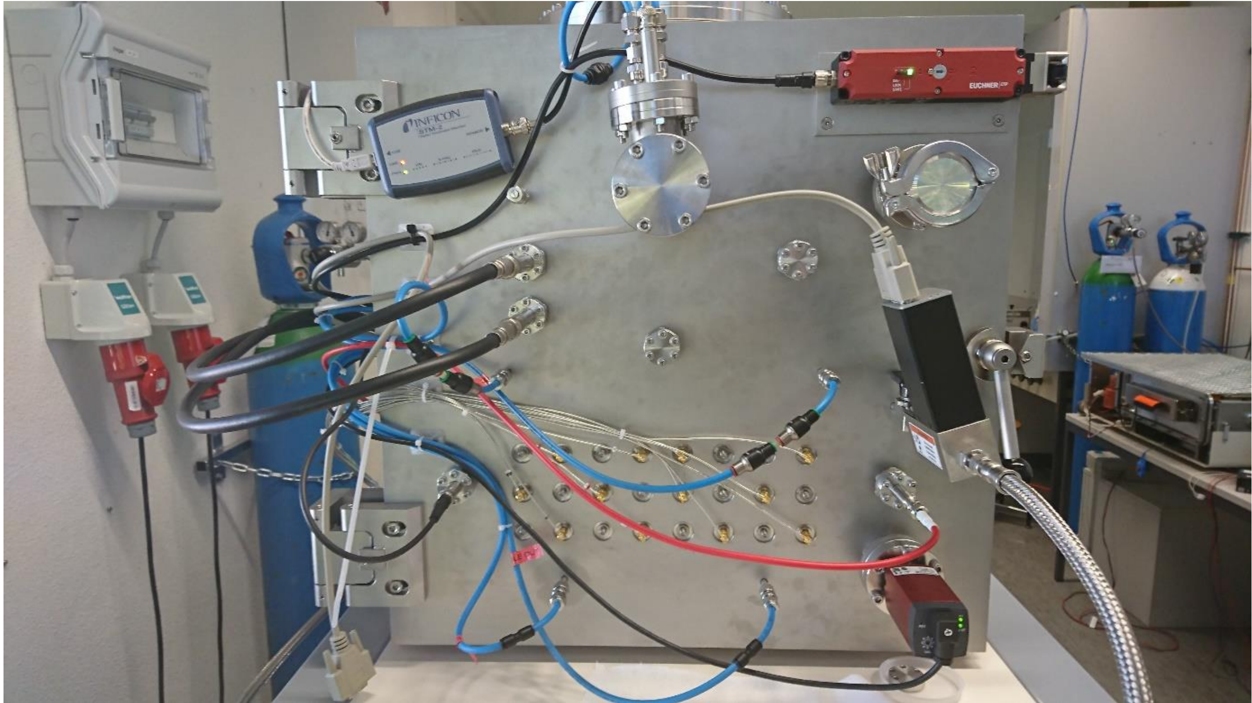

Figure 8. The vacuum chamber used in the present experiments.

CoCrFeNi MPEA thin film was processed by PVD using a Combimat Ion beam sputtering vacuum chamber manufactured by Polygon Physics. The experimental set up is exceptional among other PVD methods, because it can sputter twelve targets simultaneously (the number of targets

can be increased up to twenty four). The vacuum chamber is a steel cube with the dimensions of $50 \times 50 \times 50$ cm^3, containing the sputtering system and the target holder. The diameter of the sputtering ring between the innermost electrodes is 32 cm. The roots pump is capable of 15 m^3/h pumping, and the turbomolecular pump capacity is 0.7 m^3/s. The base vacuum in the chamber was 2×10^{-7} mbar. A schematic of the sputtering process is shown in Figure 9.

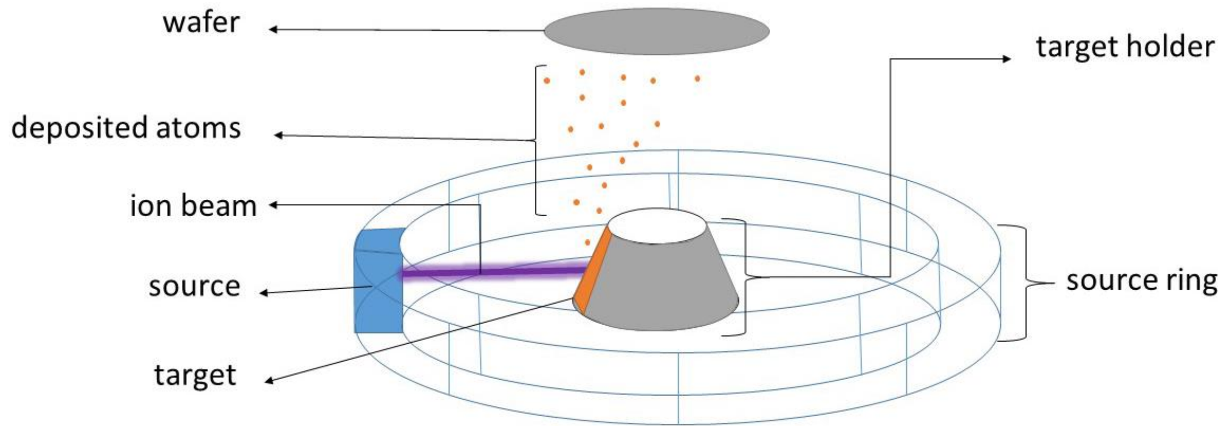

Figure 9. Schematic showing the sputtering process. Only one source and one target are shown for the simplicity.

The arrangement of the sputtering system is novel due to the compactness of the ion sources. The twelve ion sources form a ring, each one facing its own target, as shown in Figure 9. The ion energy is set by polarizing the source ring, and the ion beam shape can be controlled by polarizing the focus electrode. By controlling the ion beam shape, one can adapt the sputter spot size to the target size. These two polarizations are obtained by using two independent high voltage supplies adjustable between 0 and 15 kV. In practice, the energy of the monocharged ions produced by the sources can be tuned from 7 to 15 keV. At lower energy, the ion beams diverge and become wider than the targets used in the present experiment (it is possible to install larger targets). The repel electrode is polarized to -400V in order to deflect secondary electrons produced by the ions hitting the target (see Figure 10). Without this repel electrode, the secondary electrons are accelerated backwards to the ion sources and could damage them. The targets are fixed on the target holder, which is a massive cooled aluminum block. The sample to be coated was placed 15 cm above the target holder.

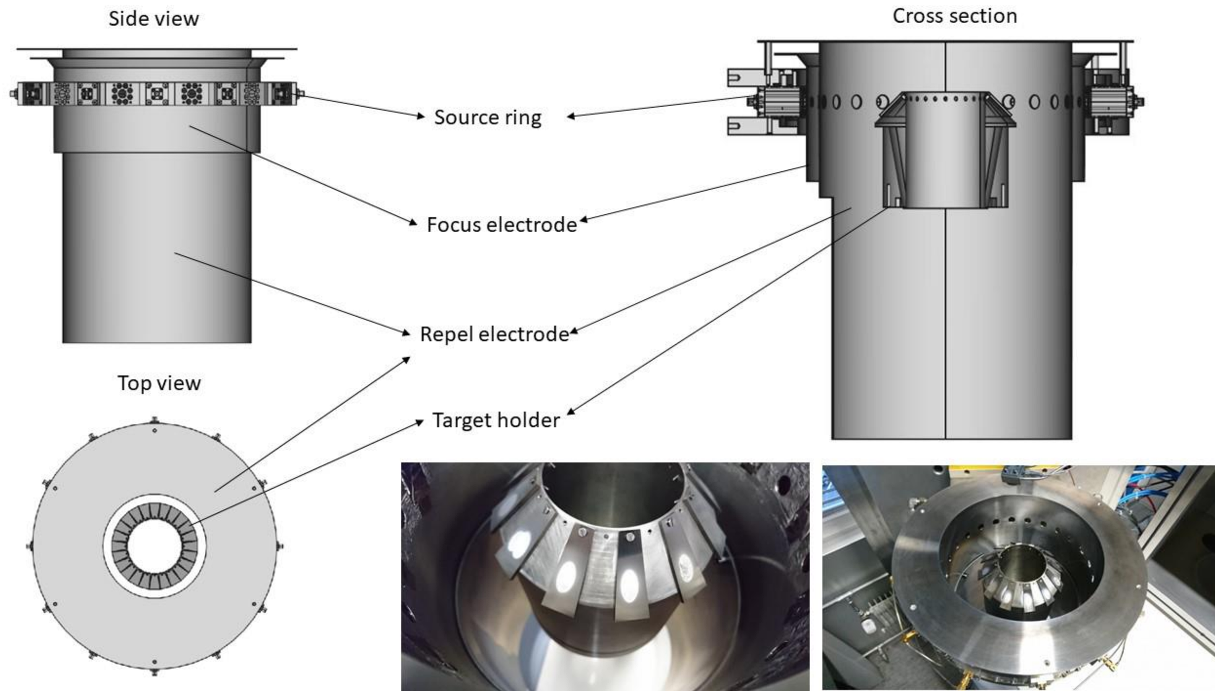

Figure 10. Schematic picture of the sputtering system.

In the present study, thin CoCrFeNi MPEA layer was sputtered on a Si single crystal substrate with the diameter of 10 cm. The substrate was on ground potential during deposition to avoid charge accumulation. The silicon wafer substrate exhibited good flatness and surface purity. The deposition lasted 21 hours. The present investigation focuses primarily on multiple beam sputtering as a candidate technology for combinatorial deposition of multicomponent thin films. Therefore, we did not investigate the adhesion between the substrate and the layer nor the effect of the substrate material on the layer microstructure in this study.

4.2. The ion source

The schematic of the ion source is shown in Fig. 11. Each source is connected to an individual solid state high frequency generator supplying the power necessary to form the plasma. The typical power feeding of each source is in the order of 3 W. By tuning this power, the extracted ion current can be set within the range of 100-500 μA. The plasma sources utilize the phenomenon of electron cyclotron resonance (ECR) [28]. In the case of ECR sources, the argon gas molecules are ionized

by the free electrons heated by the superposition of the magnetic field and the microwave. The samarium cobalt magnets in the sources provide the required magnetic field. A nonzero velocity component in a different direction will result in a cycloidal type of path for which the net drift velocity is parallel to the magnetic field lines. With the use of radio frequency, an additional oscillating electromagnetic field is created perpendicular to the original static magnetic field. When the microwave frequency matches the electron cyclotron resonance frequency, the microwave power is absorbed by the electrons. The electrons are therefore accelerated, and their kinetic energy becomes sufficient to ionize the argon atoms when they collide. Three targets from each metal were placed nearby each other to create well-defined gradients in the sample.

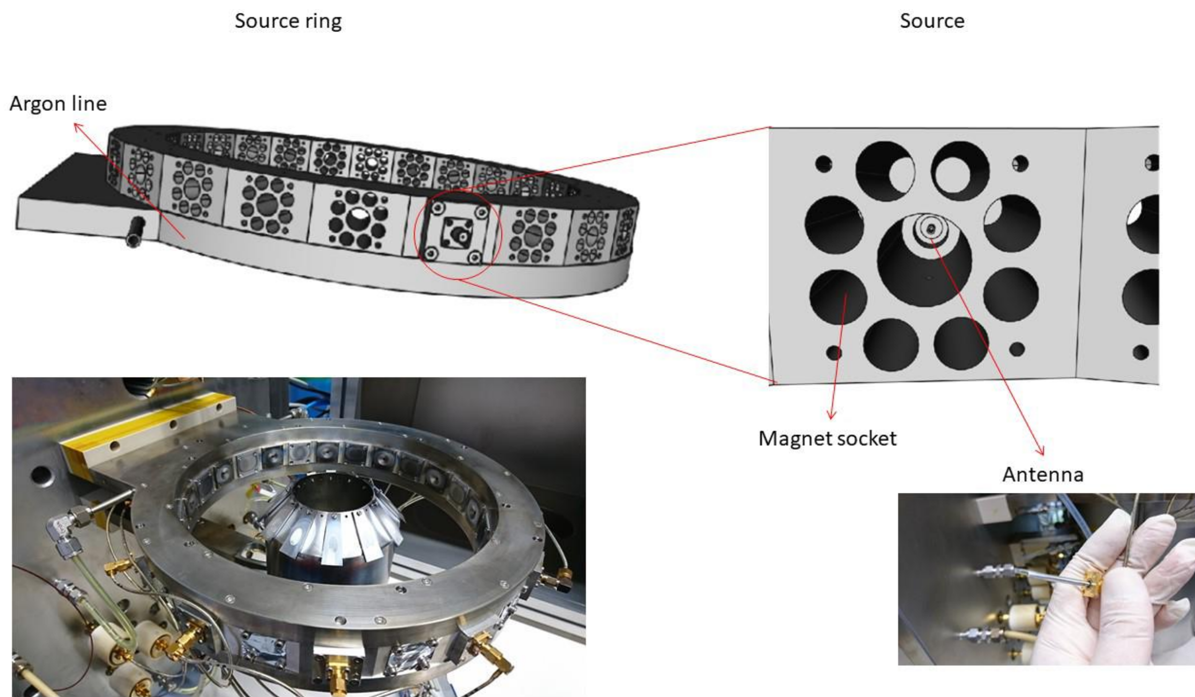

Figure 11. Schematic picture of the ion sources.

The microstructure and mechanical characterization of the sputtered film were carried out only on the part of the sample that has an equimolar CoCrFeNi composition. The results were compared with the properties of a bulk nanocrystalline CoCrFeNi MPEA sample processed by HPT. The latter sample was prepared by vacuum induction melting and drop casting of a mixture of pure metals (purity > 99.9 wt.%). A disk with a diameter of 10 mm and a thickness of ~0.85 mm was

processed by HPT using a conventional facility with quasi-constrained set-up. The processing was performed at room temperature under the pressure of 6.0 GPa and at a rotation speed of 1 rpm for 20 turns [29]. Severe Plastic Deformation (SPD) is a well known methodology to increase the mechanical strength of materials. High Pressure Torsion (HPT) is one of the most frequently used SPD technique. During this technique we place the sample between two anvils and while we apply a constant pressure on the upper anvil, the lower anvil is rotated, leading to a high strain in the material (see Figure 12). This severe deformation causes a strong grain refinement and an increase of the lattice defect density (e.g., the dislocation density).

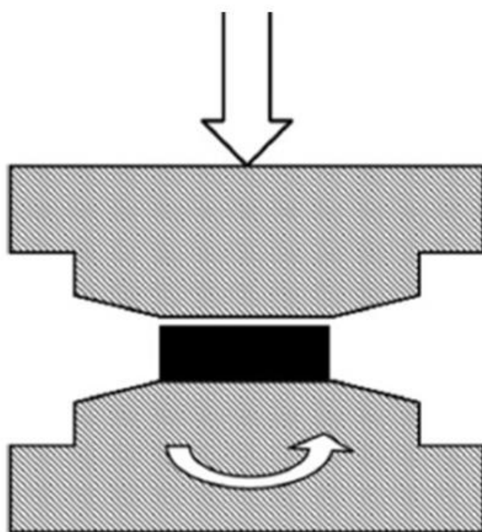

Figure 12. Schematic illustration of the HPT technique.

4.3.Analysis of the chemical composition and the film thickness

The thickness and the chemical composition of the thin film sample were measured by an X-ray fluorescence (XRF) spectrometer (type: x-ray xdv-sdd, manufacturer: Fischerscope). XRF is a non-destructive method, which is based on the phenomenon of secondary X-ray emission. When a photon hits an individual atom, an electron could be removed from orbit, leaving a vacancy behind, resulting in an excited state. When relaxation occurs, the atom emits a characteristic X-ray photon. The energy of this photon is determined by the energy levels of the orbits included in the relaxation. These photons are characteristic for each material, and from the intensities and position

of the peaks, the chemical composition of the sample could be determined. The quantity of elements also could be determined by the count of the detected signals [30]. Figure 13 shows the schematic structure of the equipment.

The studied elements ranged from aluminum to uranium. The X-ray source was a microfocus tube with a tungsten anode. The detector was a Peltier-cooled Silicon Drift Detector (SDD). The thickness and the material composition were investigated in 225 spots. Measurements were taken in a pattern consisting of 15 concentric circles with different radii. Each circle contained 15 measuring points. The diameter of each examined point was 1 mm.

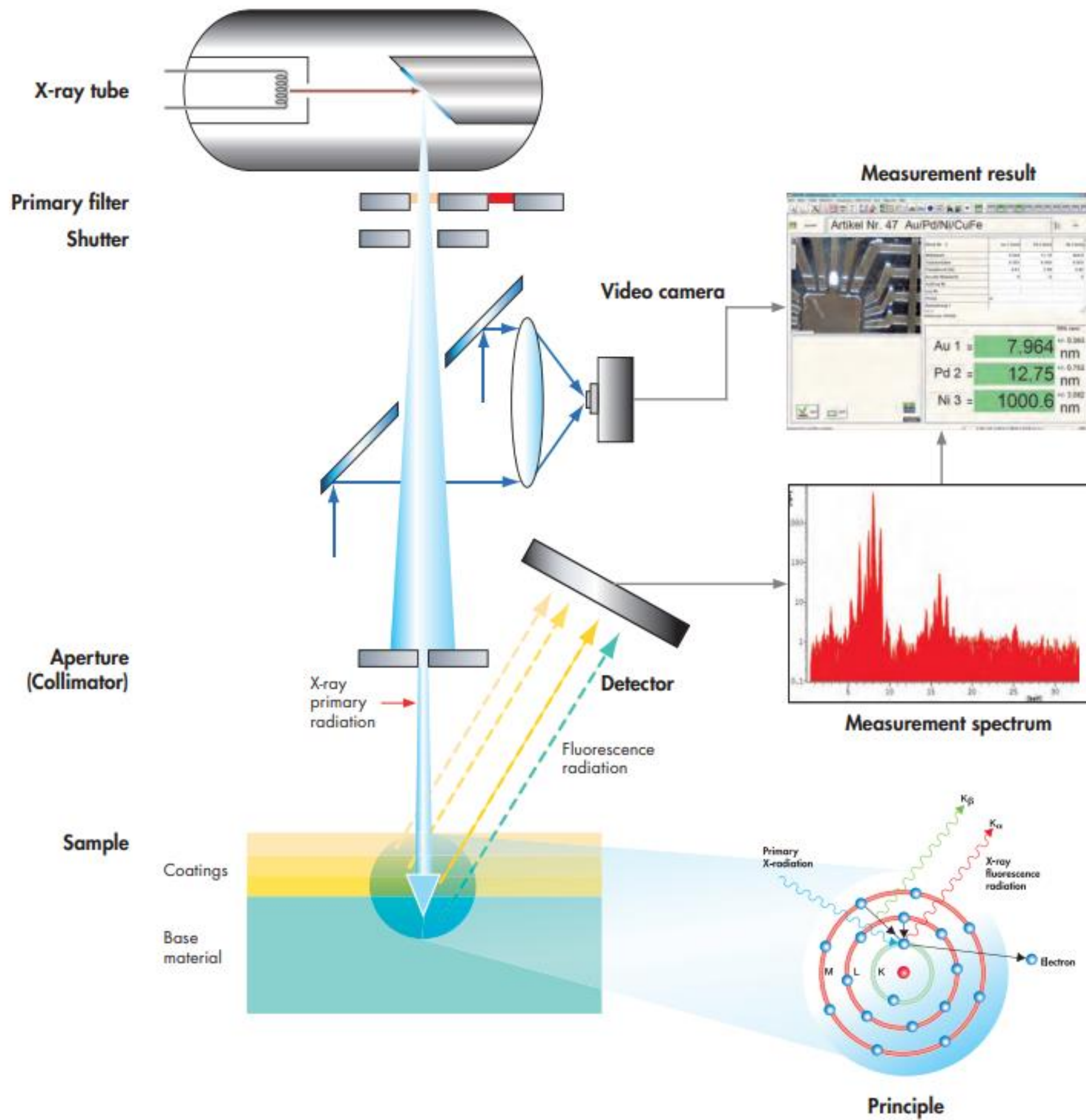

Figure 13. Schematic picture of the XRF equipment [31].

4.4. Investigation of the microstructure

4.4.1. X-ray diffraction line profile analysis (XLPA)

In the region of the PVD sample with equimolar composition, the microstructure was investigated by X-ray diffraction line profile analysis (XLPA). This is a non-destructive analytical technique, which is based on the constructive interference of monochromatic X-rays. The X-ray

was supplied from an X-ray tube, and the radiation was filtered to produce monochromatic radiation and directed to the sample. If the Bragg law is satisfied, the interaction with the sample produces constructive interferences. Due to the different lattice spacing of the different materials, it is possible to determine the phase composition and the microstructure (see Figure 14).

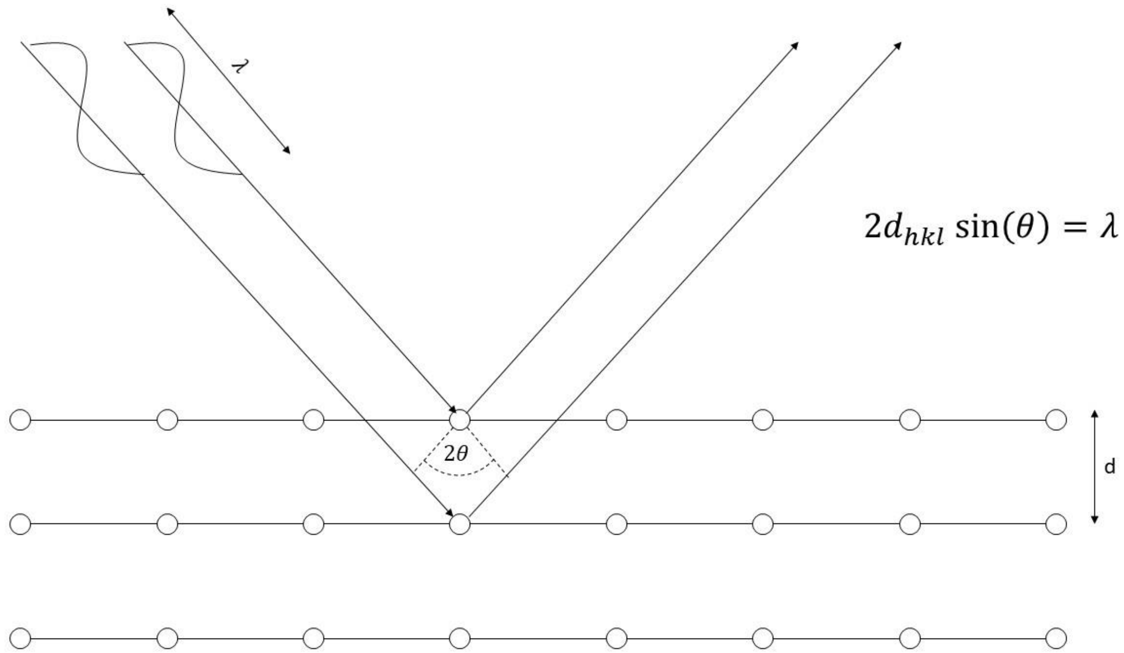

*Figure **14**. Schematic figure of the Bragg's law.*

The Bragg equation describes the relation between the X-ray wavelength (λ), the interplanar spacing (d_{hkl}) for planes (hkl) and the scattering angle (θ):

$$2d_{hkl} sin\Theta = \lambda \,. \quad (8)$$

We can determine the lattice parameter (*a*) if we index the peaks, by using the following equation which is valid for cubic structures:

$$d_{hkl} = \frac{a}{\sqrt{h^2+k^2+l^2}}. \quad (9)$$

In this work, we used an X-ray diffractometer operating at 30 kV and 25 mA with CoKα_1 radiation (wavelength: 0.1789 nm) and a single crystal Ge monochromator. The X-ray beam size was only 0.2 × 1 mm^2.

4.4.2. Transmission electron microscopy (TEM)

The microstructure was also studied by transmission electron microscopy (TEM). This is a microscopy method in which an electron beam transmitted through the sample, resulting in an image with high magnification. There are two operation modes of TEM: microscopic and diffraction modes. Depending on which pair of beams is used for projection, the result can be either an intensity image in the focal plane, called the diffraction pattern, or a real image of the sample in the image plane (Figure 15).

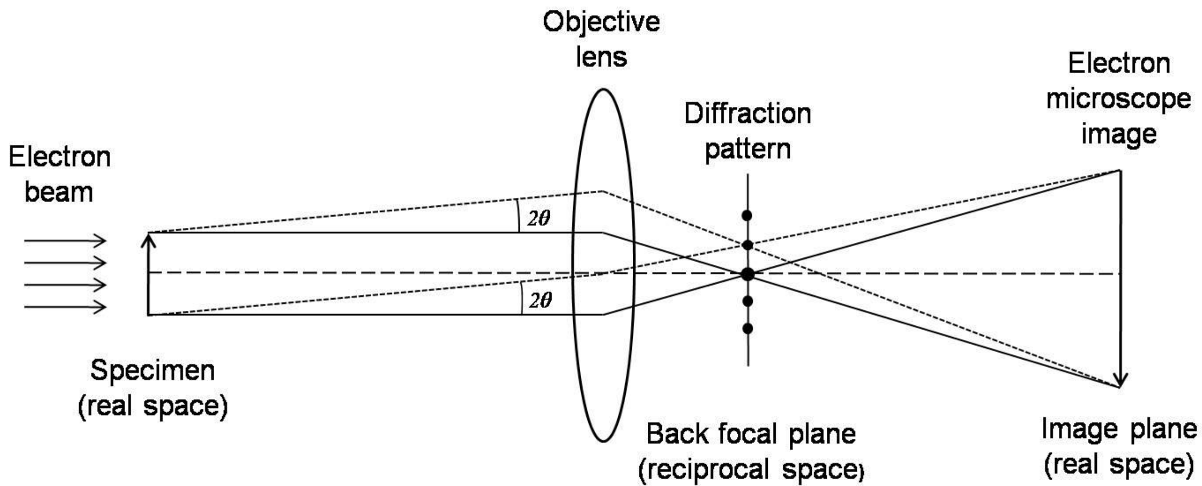

Figure 15. The optical beam diagram of TEM [32].

A TEM-lamella was cut from the sample by focused ion beam (FIB) technique using Ga ions. First, a trench around the lamella was dug using 30 keV and 30 nA until a lamella thickness of about 4 µm was obtained. Then, a thinning process was performed at a voltage of 30 keV and a current of 7 nA until a lamella thickness of 1.5 µm was achieved. Finally, the lamella was cut and transferred to a grid, where it was further thinned at 16 keV and 50 pA, followed by polishing at 5 keV and 48 pA, and finished at 2 keV and 27 pA. TEM bright-field (BF) and dark-field (DF)

images were taken by a Titan Themis G2 200 transmission electron microscope. The TEM images were recorded at 200 keV with a 4k*4k CETA 16 CMOS camera controlled by VELOX software. The TEM experiments were performed by Dr. János Lábár (ELKH EK MFA).

4.4.3. Pole figure measurement

The crystallographic texture of the sample was characterized by pole figure measurements using a Smartlab X-ray diffractometer (manufacturer: Rigaku, Japan) with CuKα radiation (wavelength: 0.15418 nm) and parallel-beam optics. In the case of pole figure measurement, a single Bragg condition is maintained between the source and the detector for a set of planes, and the sample was tilted through all the possible orientations in the top hemisphere. The schematic representation of this measurement can be seen in Figure 16. The α angle represents the tilt of the scattering vector $\boldsymbol{g}$ around the unit normal between 0 and $\frac{\pi}{2}$. β is the rotation of the $\boldsymbol{g}$ vector around the unit normal between 0 and 2π. Scanning all the possible values of α and β provides a map for different intensities, which can be related to the number of reflecting crystallites. The intensities measured for every tilt of the scattering vector can be projected to a plane map. The most used type of projection is a flat circular projection commonly used to visualize the obtained data.

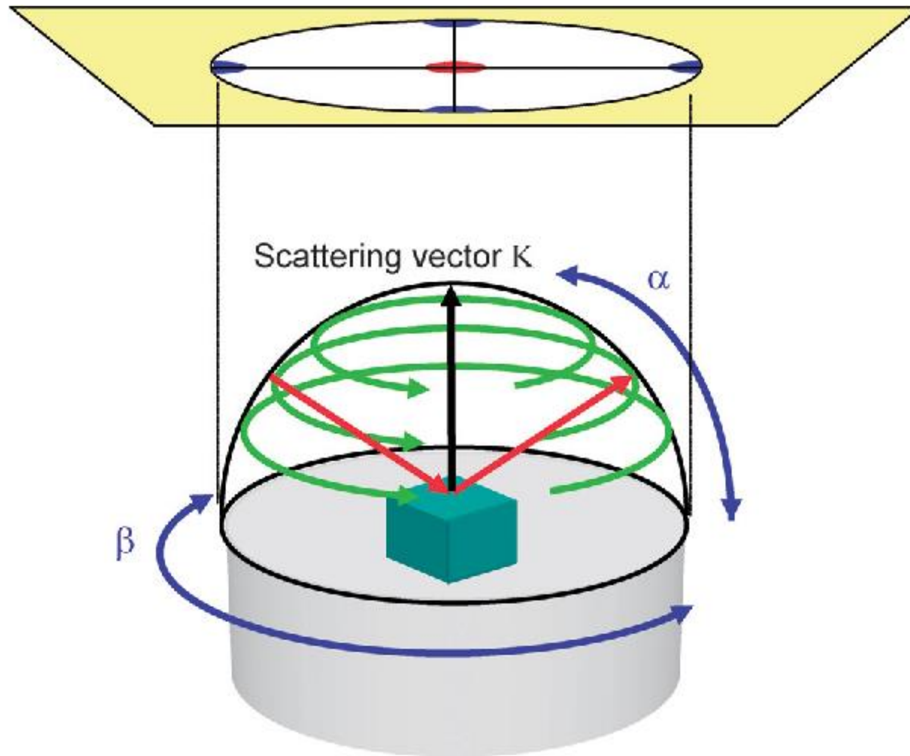

Figure 16. Schematic representation of the pole figure measurement [33].

4.5. Nanoindentation

Nanoindentation measurements were performed using a Hysitron Ubi nanoindenter equipped with a diamond Berkovich tip. This hardness measurement method is fundamentally on the nanoscale. In this technique, a hard tip penetrates the sample while the equipment measures the load and the displacement of the tip while the loading and unloading rate kept constant. In the present study, a Berkovich tip was used which can be seen in Figure 17.

Berkovich indenter

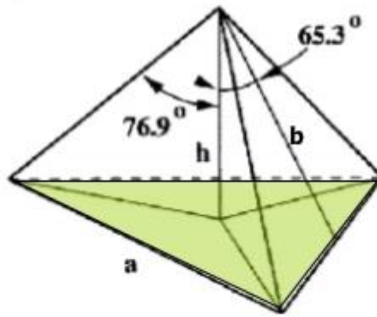

$$\tan 60^o = \frac{l}{a/2}$$

$$l = \frac{\sqrt{3}}{2}a$$

$$A_{proj} = \frac{al}{2} = \frac{\sqrt{3}}{4}a^2$$

$$\cos 65.27^o = \frac{h}{b}$$

Projected area

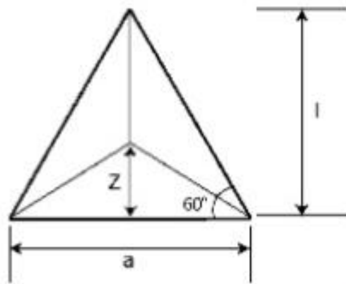

$$h = \frac{a\cos 65.3^o}{2\sqrt{3}\sin 65.3^o} = \frac{a}{2\sqrt{3}\tan 65.3^o}$$

$$a = 2\sqrt{3}h\tan 65.3^o$$

$$A_{proj} = 3\sqrt{3}h^2\tan^2 65.3^o = 24.56h^2$$

Figure 17. Berkovich tip with its area (A_{proj}) versus indentation depth (h) function.

This technique is suitable to obtain three properties of the sample: stiffness, hardness, and the Young's modulus (elastic modulus). The stiffness is the rigidity of an object. This quantity can be obtained as the derivative of the beginning of the unloading curve.

$$S = \frac{dP}{dh}, \tag{10}$$

where P is the load, and h is the displacement of the tip. The hardness of a sample describes the resistance of the material to a permanently applied mechanical load. In equation (11), P_{max} is the highest applied load, and A_c is the so-called residual contact area of indentation:

$$H = \frac{P_{max}}{A_c}. \tag{11}$$

A_c can be used to obtain the elastic modulus of the sample. Then, the reduced modulus can be obtained as:

$$E_r = \frac{\sqrt{\pi}}{2} \frac{S}{\sqrt{A_c(h_c)}}, \quad (12)$$

where β depending on the tip shape. The reduced modulus can be related to the Young's moduli and the Poisson's ratios of the sample (E and v) and the indenter (E_i and v_i) as:

$$E_r = \left(\frac{1-\nu^2}{E} + \frac{1-\nu_i^2}{E_i} \right)^{-1}. \quad (13)$$

The maximum load applied in these experiments was 3 mN in order to avoid exceeding a maximum penetration depth of 100 nm. The loading and unloading parts of indentation took 5-5 s, and the holding time at the maximum load was 2 s. The hardness and the elastic modulus were determined by applying the Oliver-Pharr method [34]. The area function for the tip had been calibrated carefully before the start of the measurements for the relevant measurement range. 25 indents were made on both the PVD film and the bulk sample to obtain a conclusive average.

5. Results and discussion

5.1. The spatial distribution of the film thickness and the chemical composition

Figure 18 shows the thickness map of the thin film as obtained by XRF. The average thickness of the sample was 0.799 µm with a standard deviation of 0.086 µm. The maximum thickness was measured as 0.916 µm close to the edge of the sample near the Co source. The variation of the thickness of the PVD film was caused by the different sputtering rates of the various targets.

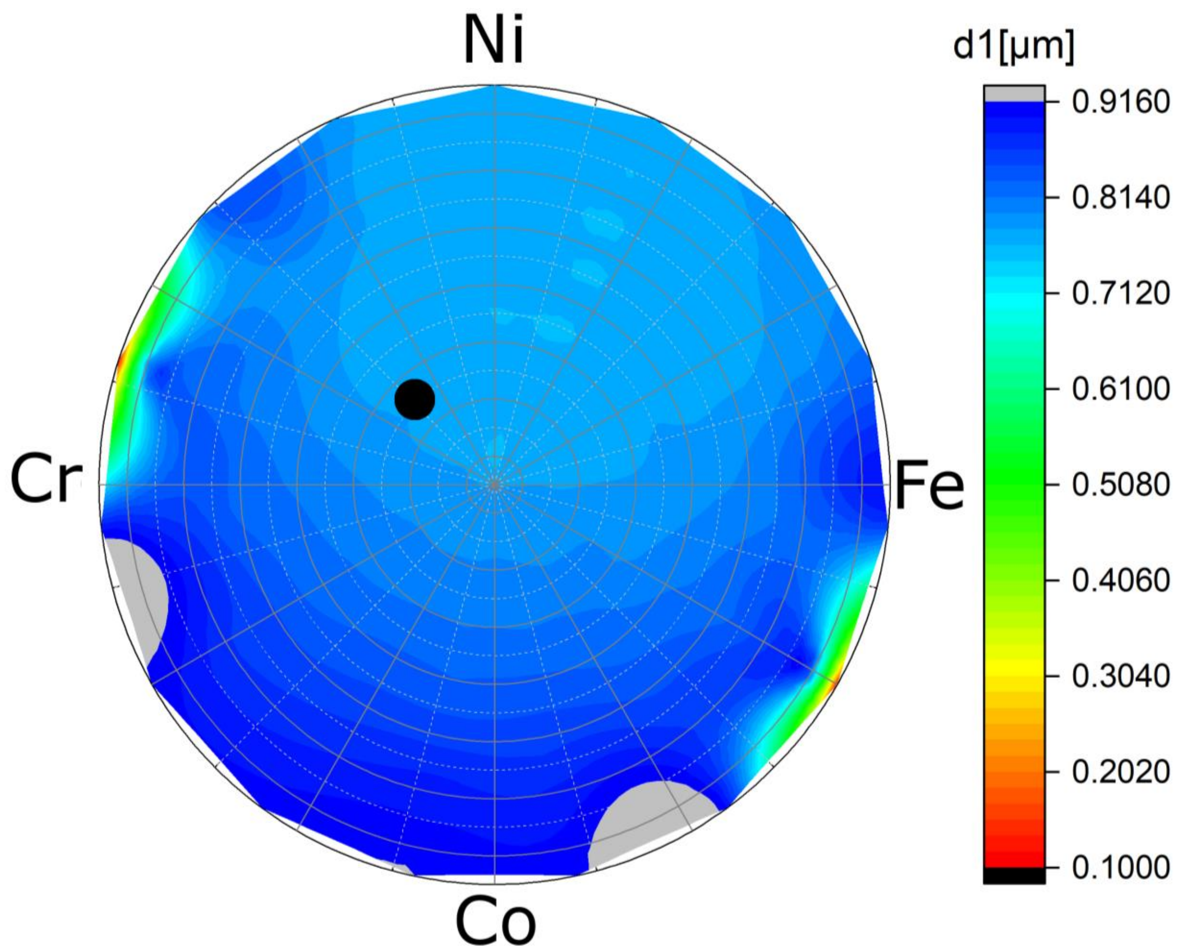

Figure 18. The thickness map of the thin film. The equimolar space is indicated by a black spot.

The distribution of the concentrations of the constituents on the surface of the sample obtained by XRF is shown in Figure 19. Owing to the circular arrangement of the targets around the substrate and the plume shape sputtering, the elements show a gradient distribution. It is important to note that due to the different sputtering rates, the place having equimolar composition slightly moved from the center away from the Co source as indicated by the black spot in Figure 19. The concentration distributions of the different elements are shown in Figure 20. The concentration of each element varies in a range between ~5 and ~50 at.%. The peaks of the concentration distributions can be found at ~25 at.% for Cr and Fe while these peaks are at about 30 and 20 at.% for Co and Ni, respectively. The higher peak concentration for Co can be explained by its higher sputtering rate. The Ni source was located on the opposite side of the PVD chamber, which can explain its lower peak concentration.

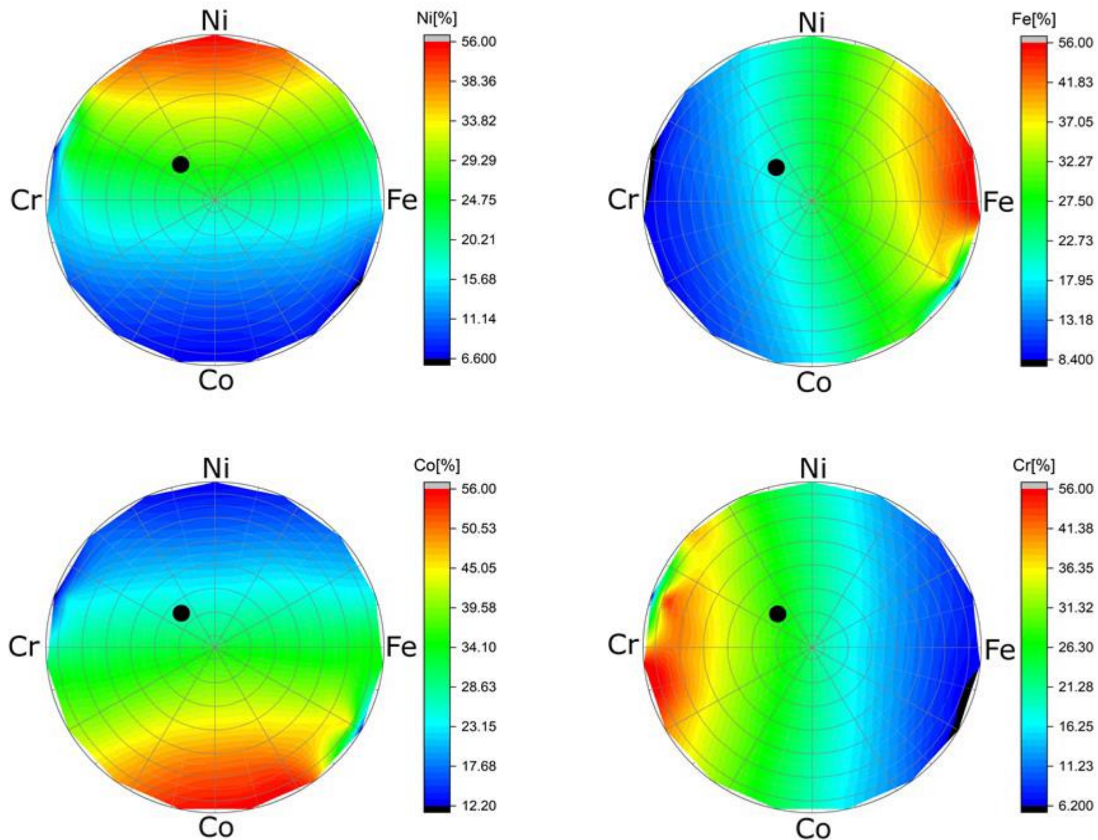

Figure 19. Color maps of the distribution of the concentrations of the constituents in the sample. The equimolar space is indicated by a black spot.

The equimolar concentration point can be found between the center of the wafer and the Ni source. In this work, we investigate the microstructure only in the spot corresponding to the equimolar CoCrFeNi because the results are intended to compare with the data available in the literature for the same MPEA composition but processed by a different technique. The width of this "equimolar concentration" spot was 1 mm, with the condition that the concentration of each element must be within the range of 24-26 at%.

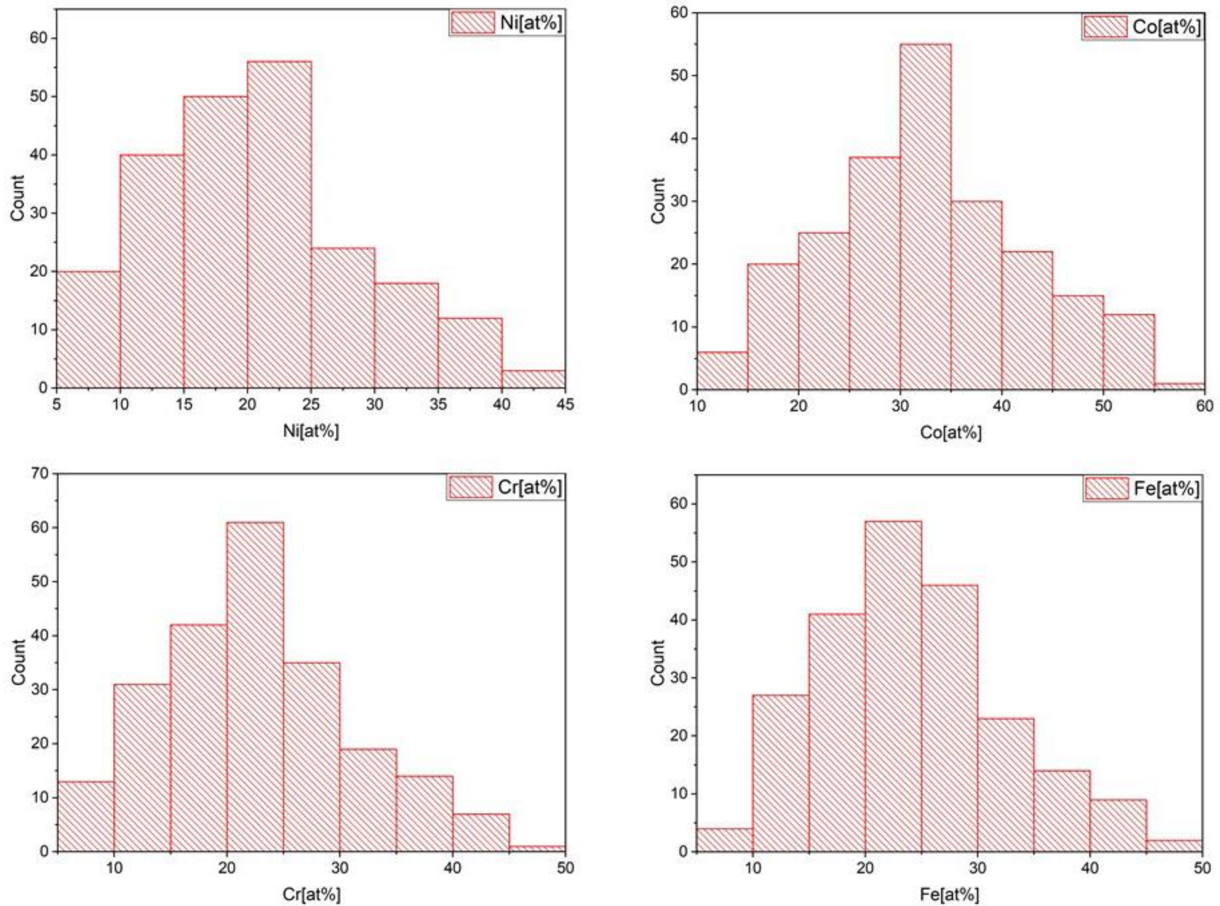

Figure 20. The distribution of the concentrations of the four constituents in the PVD sample. These distributions were constructed from the color maps in Figure 19.

5.2. Crystallite size and texture of the equimolar CoCrFeNi film

The X-ray diffraction pattern taken in the part of the sample with equimolar composition indicated that the material is a single phase face centered cubic (fcc) structure. The full width at half maximum (FWHM = $\cos\theta*\Delta 2\theta/\lambda$, where θ is the Bragg angle of the reflection, $\Delta 2\theta$ is the breadth of the peak in radians and λ is the wavelength of X-rays) was determined for each peak and plotted as a function of the magnitude of the diffraction vector ($g = 2*\sin\theta/\lambda$). These Williamson-Hall plots for the samples processed by PVD and HPT are shown in Figure 21.

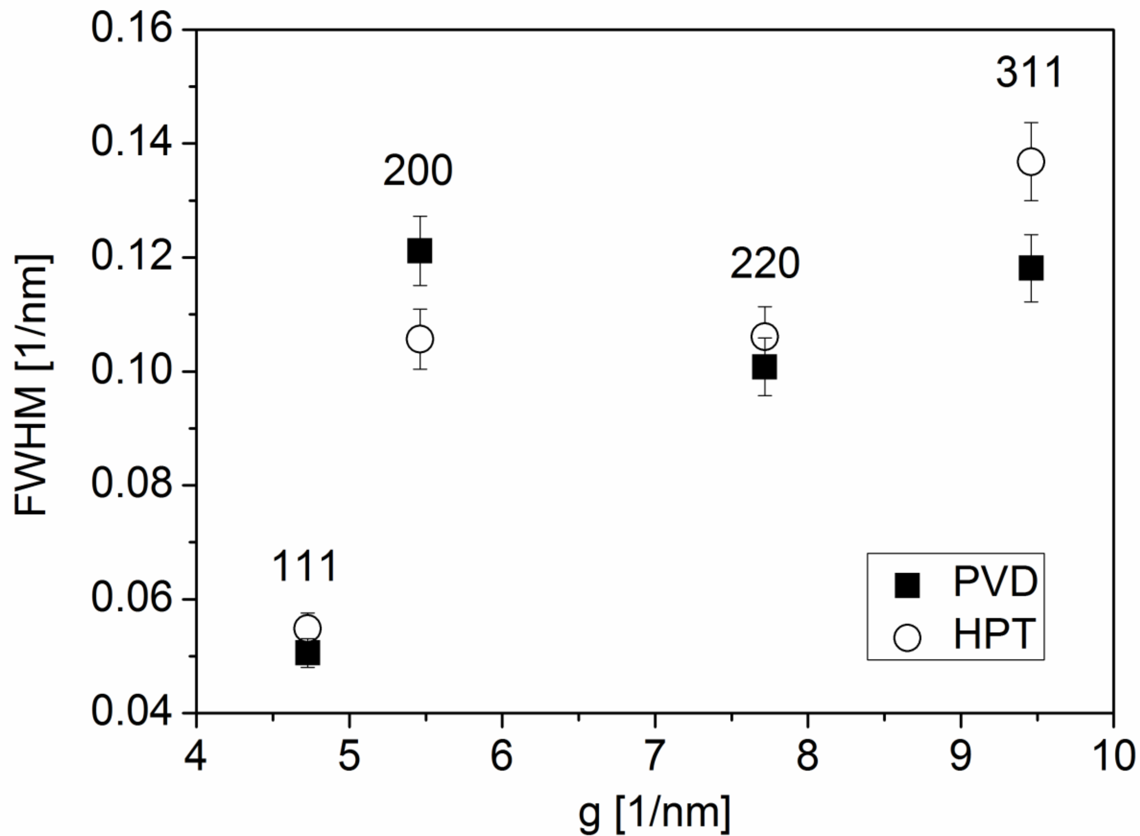

Figure 21. The Williamson-Hall plot of the two CoCrFeNi MPEA samples processed by PVD and HPT.

Only slight differences were observed between the Williamson-Hall plots of the two samples. X-ray diffraction peaks can broaden due to the small crystallite size, the lattice defects

such as dislocations and stacking/twin faults, as well as chemical heterogeneities [35]. A small spot size of the X-ray beam was selected (see section 4.4.1), and hence, the influence of chemical heterogeneities can be assumed to be marginal. The contribution of lattice defects to peak broadening increases with increasing the magnitude of the diffraction vector. Thus, the apparent crystallite size (*d*) was determined as the reciprocal of the breadth of the first diffraction peak with the indices *111* ($FWHM_{111}$) in accordance with the Scherrer formula [35]:

$$d = \frac{1}{FWHM_{111}} \tag{14}$$

The crystallite size for both, the PVD- and HPT-processed samples was determined to be around 20 nm, i.e., the two essentially different top-down and bottom-up methods gave similar microstructures.

The 111 pole figures in Figure 22 reveal that both PVD- and HPT-processed specimens exhibit similar textures where planes {111} are lying parallel to the sample surface. In the case of the HPT specimen, this texture was formed due to severe plastic deformation occurring during the 20 turns. For the PVD film, the 111 texture can be explained by the lowest surface energy if planes 111 are oriented parallel to the layer surface. The lower overall intensity in the pole figure of the PVD sample was caused by the smaller studied volume since the film thickness (~1 µm) was lower than the penetration depth of X-rays. Nevertheless, it is evident from Figure 22 that the texture is sharper for the PVD film than in the case of the HPT-processed CoCrFeNi MPEA.

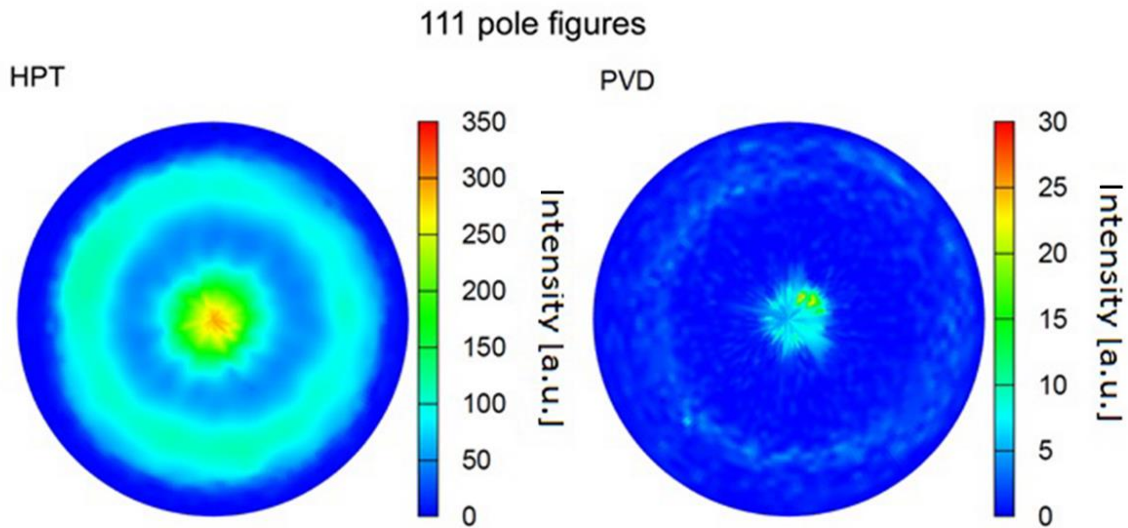

Figure 22. 111 pole figures for the two CoCrFeNi MPEA samples processed by PVD and HPT.

5.3. Study of the microstructure by TEM

Figure 23a shows a BF image for the cross section of the PVD-processed MPEA film at the equimolar concentration spot. The average thickness of the layer as determined from the TEM images was 720 nm, which is in good agreement with the value obtained by XRF technique (see Fig. 18). The surface of the film was relatively smooth as revealed by the TEM image in Fig. 23a. The uncertainty of the layer thickness was about 10 nm which reflects the roughness of the film surface. The DF micrograph in Fig. 23b reveals that the layer consists of columns perpendicular to the film surface with the thickness varying between 20 and 100 nm. The inset in Fig. 23b shows the corresponding selected area diffraction pattern. The development of the columnar grain structure can be explained by the oriented film growth perpendicular to the substrate surface during PVD.

Figs. 23c and d show BF and DF TEM images, respectively, with higher magnification. The bright and dark spots in Fig. 23d suggest that the columns are fragmented into grains/subgrains. Their average size was found to be ~17 nm after studying about one hundred

grains/subgrains. This value is in reasonable agreement with the crystallite size determined from the X-ray diffraction peak breadth (~20 nm, see section 5.2).

Figures 24a and b show BF and DF micrographs obtained for the bulk CoCrFeNi MPEA sample processed by HPT. The average grain size was about 80 nm as determined from the TEM images. The inset in Fig. 24b shows the corresponding selected area diffraction pattern. A part in Fig. 24b was magnified in Fig. 24c, revealing that the grains consist of subgrains with a similar size as the crystallite size obtained by the analysis of the X-ray diffraction peak breadth (~20 nm). Thus, it seems that for both PVD- and HPT-processed samples the microstructure is fragmented into crystallites and the sizes of these crystallites are very similar for the two materials.

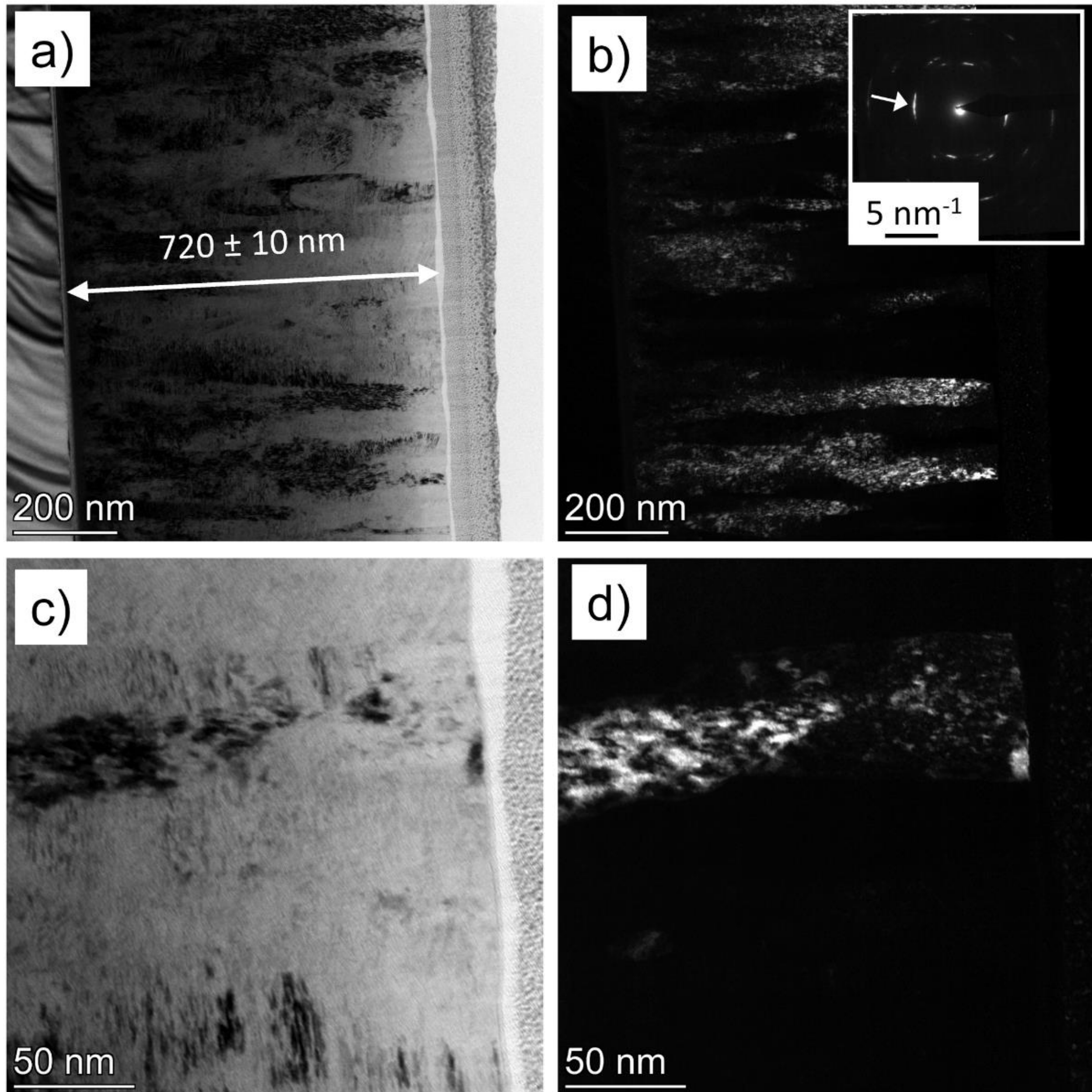

Figure 23. BF (a, c) and DF (b, d) TEM images taken on the cross section of the PVD-processed CoCrFeNi MPEA film. The Si substrate is at the left side of the images in (a) and (b). The micrographs in (a) and (b) show the columnar microstructure while the images in (c) and (d) reveal the fragmentation of the columns into smaller grains/subgrains. The inset in (b) shows the corresponding selected area diffraction pattern. The arrow in the inset indicates the diffraction spot used for taking the DF images.

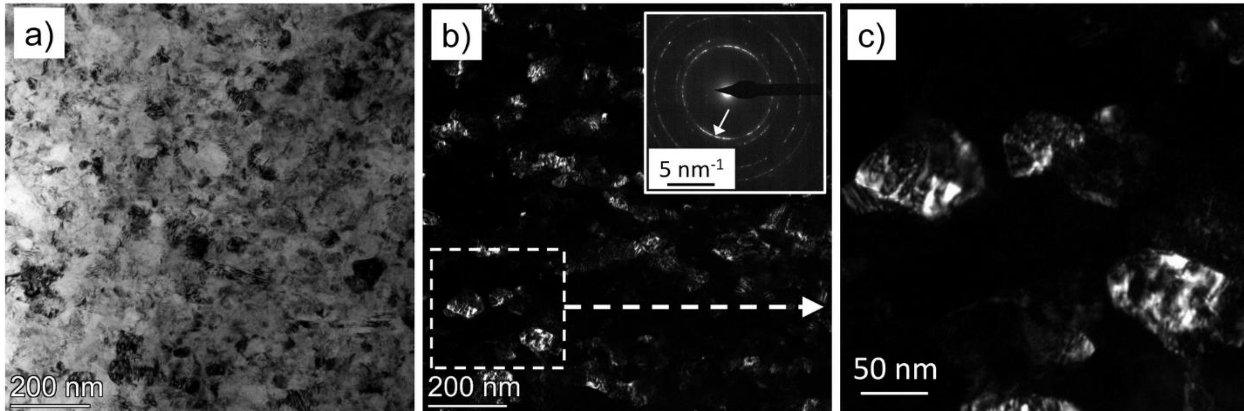

Figure 24. BF (a) and DF (b) TEM images taken on the bulk CoCrFeNi MPEA sample processed by 20 turns of HPT. A magnified part of (b) is shown in (c) which suggests that the grains are fragmented into smaller subgrains. The inset in (b) shows the corresponding selected area diffraction pattern. The arrow in the inset indicates the diffraction spot used for taking the DF image.

5.4. Comparison of the nanohardness obtained for PVD- and HPT-processed CoCrFeNi MPEAs

Figure 25 shows the load – penetration depth curves from the nanoindentation measurements. The indentation experiments were performed by Dr. Nadia Rohbeck. The Hysitron nanoindenter operates in load control mode and before starting the hardness tests, measurements with different loads have been performed in order to establish the load related to a maximum penetration depth of 100 nm. This depth value is about one order of magnitude smaller than the film thickness which guarantees to avoid any substrate effect on the measured hardness and elastic modulus.

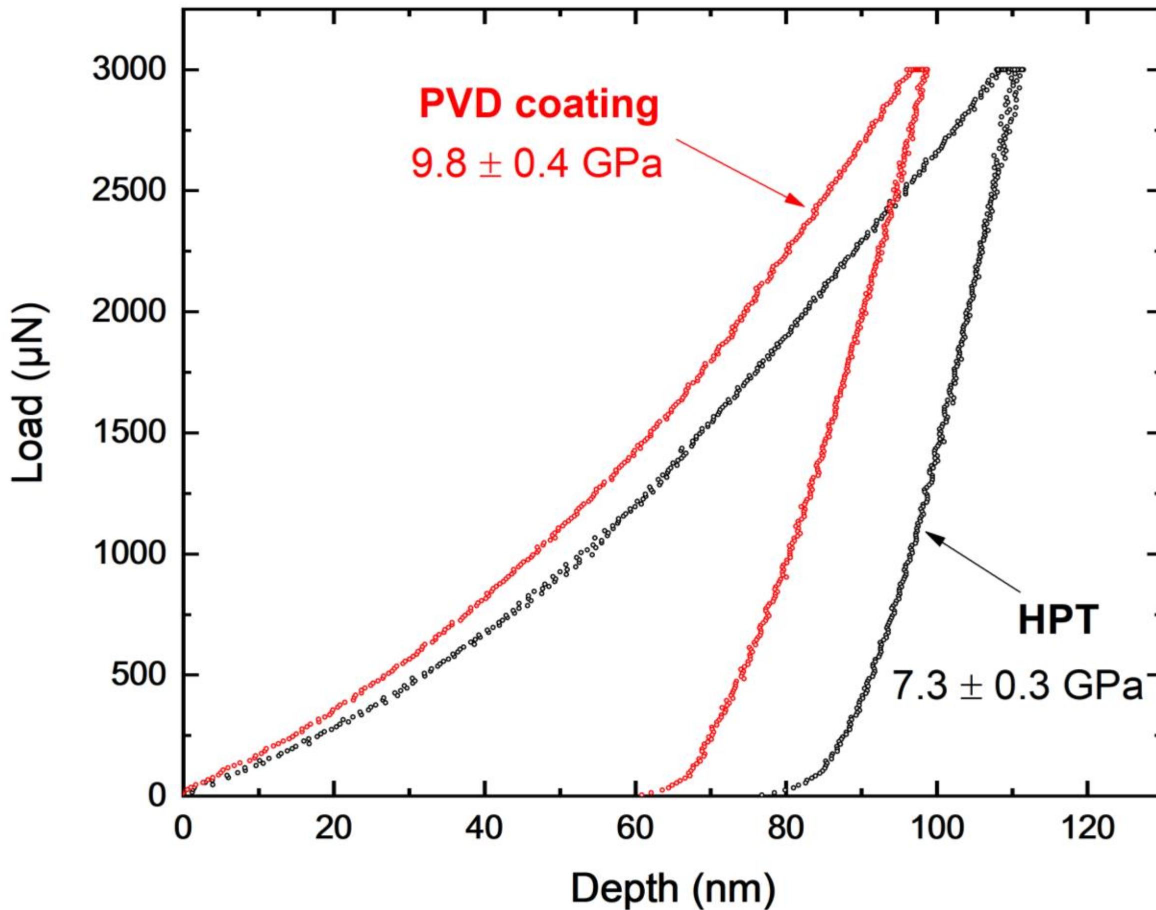

Figure 25. Load-penetration depth curves obtained by nanoindentation for the samples processed by PVD and HPT.

The average hardness of the PVD film was 9.8 ± 0.4 GPa which is notably higher than that obtained for the bulk counterpart processed by HPT (7.3 ± 0.3 GPa). The higher hardness of the PVD sample cannot be attributed to any difference in the crystallite size or the defect densities (e.g., dislocation density or stacking fault and twin fault probabilities) since the PVD and HPT samples have very similar Williamson-Hall plots. TEM also revealed that the average size of the smallest microstructural units, i.e., the subgrains, is very similar for the two materials. At the same time, the pole figures in Figure 22 indicate a significant difference between the textures of the two samples. Although, both samples have a 111 texture, the PVD film shows a sharper texture compared to the sample processed by HPT. This difference may cause the higher hardness of the PVD sample as 111 texture yields the highest hardening effect among all of the possible

crystallographic directions if the material is loaded perpendicular to the investigated surface [36]. Indeed, former studies (e.g., [37]) showed that 111 texture in fcc films yields a higher hardness compared to other preferred crystallographic orientations. The Young's moduli determined from the present nanoindentation were 233 GPa and 276 GPa for the PVD film and the bulk MPEA sample, respectively. Considering the error of these values (~10%), significant difference was not found between the moduli of the two samples. Moreover, these Young's moduli are close to the values calculated and measured for bulk CoCrFeNi MPEA (250 ± 30 GPa) in the literature [38]. It seems that the elastic modulus is less sensitive to the 111 texture than the hardness for the present MPEA which is in line with former studies. Indeed, it has been revealed that the weakening of 111 texture has a more pronounced effect on the flow stress through the variation of the Taylor factor than on the Young's modulus (compare Figs. 4 and 6 in Ref. [36]). In addition, indentation testing is a multiaxial deformation which also moderates the influence of texture on the measured modulus.

It should be emphasized that the present PVD sample exhibited a higher hardness than the values reported for CoCrFeNi MPEA in previous studies. In Table 1, a direct comparison between the results obtained here and the literature data is given. Huo et al. [39] measured the hardness of equimolar CoCrFeNi samples processed by arc melting and subjected to tensile deformation. The obtained values were between 3.4 and 3.8 GPa, which are much lower than the hardness determined for the present PVD film. This difference can be explained by the much larger grain size (200-300 μm) of the arc melted samples compared to that of the films studied here (about 20 nm). In another study, Sathiyamoorthi et al. [40] fabricated CoCrFeNi composite samples with chromium-oxide and carbide particles using a combined approach of mechanical alloying (MA) of powders and subsequent spark plasma sintering (SPS). The grain size of the as-consolidated composite was ~120 nm and the hardness was measured to be about 5.7 GPa. In the present study, the much higher hardness can be attributed to the smaller grain size of ~20 nm and the 111 texture (see the previous paragraph). It should be noted, however, that the load applied during the hardness test also influences the measured hardness value. Due to the small thickness of the PVD film, only a low load (3 mN) could be applied during the hardness test. This force is orders of magnitude smaller than the loads used for bulk samples in the literature (see Table 1). Therefore, the so-called indentation size effect (ISE) might also contribute to the higher hardness measured in the present study. The essence of this phenomenon is that the lower the load (and therefore the indentation

size), the higher the hardness measured for the same material [41]. Nevertheless, the present study demonstrated the possibility of processing hard CoCrFeNi MPEA film by multiple beam sputtering in PVD using commercially pure metal targets.

Table 1. Comparison between the grain sizes and the hardness values obtained in this study and the literature data for CoCrFeNi MPEA. It is noted that the material listed in the second row of the table was a composite with MPEA matrix and chromium-oxide and carbide particles which were formed during SPS sintering.

Reference	Starting material	Processing	grain size	Hardness (load)
Huo et al. [37]	Co, Cr, Fe, Ni high-purity metal	arc melting	~200-300 µm	3.4-3.8 GPa (100 mN)
Sathiyamoorthi et al. [39]	Co, Cr, Fe, Ni high-purity powder	MA and SPS	~120 nm	5.7 GPa (9.8 N)
present work	Co, Cr, Fe, Ni high-purity metal	multi ion beam sputtering	~20 nm	9.8±0.4 GPa (3 mN)
		HPT	~20 nm	7.3±0.3 GPa (3 mN)

As this novel technique produces combinatorial samples with a significant spatial distribution of constituents, the as-processed film allows to study the influence of chemical composition on the structure and properties of MPEAs. Since the composition varies continuously in the as-processed samples, this method facilitates the effort towards finding the optimum composition with the required properties. This optimization process is easier and faster compared to other methods where for each composition an individual sample must be prepared. It is also noted that the number of components can be scaled up to twelve as this PVD system can sputter

twelve targets simultaneously. However, the main objective of this work was to demonstrate the ability of the present multibeam sputtering technique to deposit MPEA thin film systems. Therefore, only the spot with an equimolar composition was studied and compared with a bulk counterpart processed by SPD. In our next study, the effect of the chemical composition on the structure and the hardness in the Co-Cr-Fe-Ni MPEA system will be studied on a combinatorial sample processed with this new PVD technique.

6. Conclusions

The microstructure, the texture and the hardness of a CoCrFeNi MPEA thin film processed by a novel multibeam sputtering PVD technique were investigated. This method does not require preliminary manufacturing of MPEA targets as it can sputter commercially pure metal targets. The following results were obtained:

1. The elements in the alloy have a well-defined gradient, which is the consequence of the specific geometry of the multiple beam sputtering system. With the application of this PVD method, we created a CoCrFeNi MPEA thin film with the thickness of about 1 μm. A spatial distribution of the elemental concentrations within the range of 5-50 at. % was observed. This new processing technique is capable of producing combinatorial samples that allows studying the effect of chemical composition on the structure and properties of multicomponent alloys.

2. The crystallite size was determined by X-ray line profile analysis. The PVD thin film and the HPT bulk material both had a crystallite size about 20 nm. The two essentially different bottom-up and top-down method produced similar microstructure.

3. The texture of the multibeam sputtered MPEA thin film and the HPT bulk material was obtained by pole figure measurement. Both samples displayed a 111 texture, but the thin film had a significantly sharper texture.

4. The morphology of MPEA thin film was investigated by transmission electron microscopy. The microscopy revealed that the layer consists of columns perpendicular to the film

surface with the thickness varying between 20 and 100 nm. The development of the columns could be explained by the synthetizing method.

5. The hardness of the equimolar CoCrFeNi MPEA thin film sputtered by this PVD method was 9.8 ± 0.4 GPa, which is outstanding among the values obtained for similar CoCrFeNi MPEAs processed by other techniques in the literature. This exceptionally high hardness is likely due to the small grain size of ~20 nm. The reference sample was a HPT-processed bulk nanocrystalline CoCrFeNi MPEA, which exhibited a lower hardness (7.3 ± 0.3 GPa) even though it had the same crystallite size. The significantly larger hardness of the PVD film was attributed to the sharper 111 texture developed due to the columnar growth of the layer.

7. The contributions of the author

I participated in the evaluation of all the data that appear in this thesis. I carried out the synthesis of the MPEA sample and the XRF measurements and maintained the PVD equipment. I also participated in the improvement of the PVD instrument, which included the installation of the repel electrode.

8. Outlook

The research mentioned at the end of the fifth chapter is already in progress. We are using synchrotron X-ray diffraction to create a diffraction map for one of these gradient samples, thereby we can examine the changes of the microstructure and phase composition as a function of the chemical composition. We plan to use advanced methods in our evaluation process such as neural network assisted classification of the diffractograms. The main focus of this research is to get a better understanding of the changes in the mechanical properties of MPEA thin films as a function of microstructure.

Although this work is only in progress, I would like to introduce a few of our results and demonstrate the research potential of this topic. In Figure 26, we can see the element distributions

in the sample used in the continuation of this research. In that work, we are going to focus on the combinatorial aspect of this sample which could be investigated very effectively with synchrotron X-ray diffraction since we can measure the sample with a high resolution. The diffraction measurements have already been finished, we measured 1100 point in the sample. This give us the opportunity to virtually select any point of the sample for investigation, which provide a great range of combination of composition of the MPEA sample. For example, in Figure 27 three points were selected on the wafer and the corresponding diffractograms were plotted.

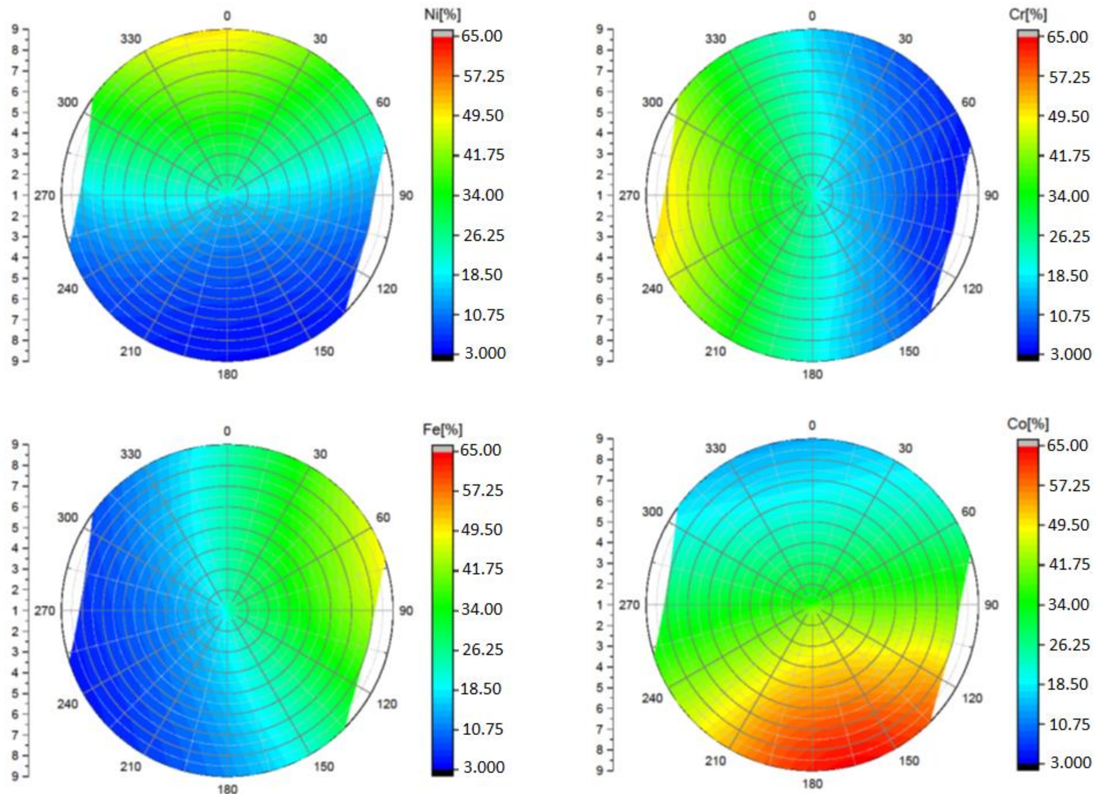

Figure 26. Color maps of the distribution of the concentrations of the constituents in the sample used in the continuation of this research.

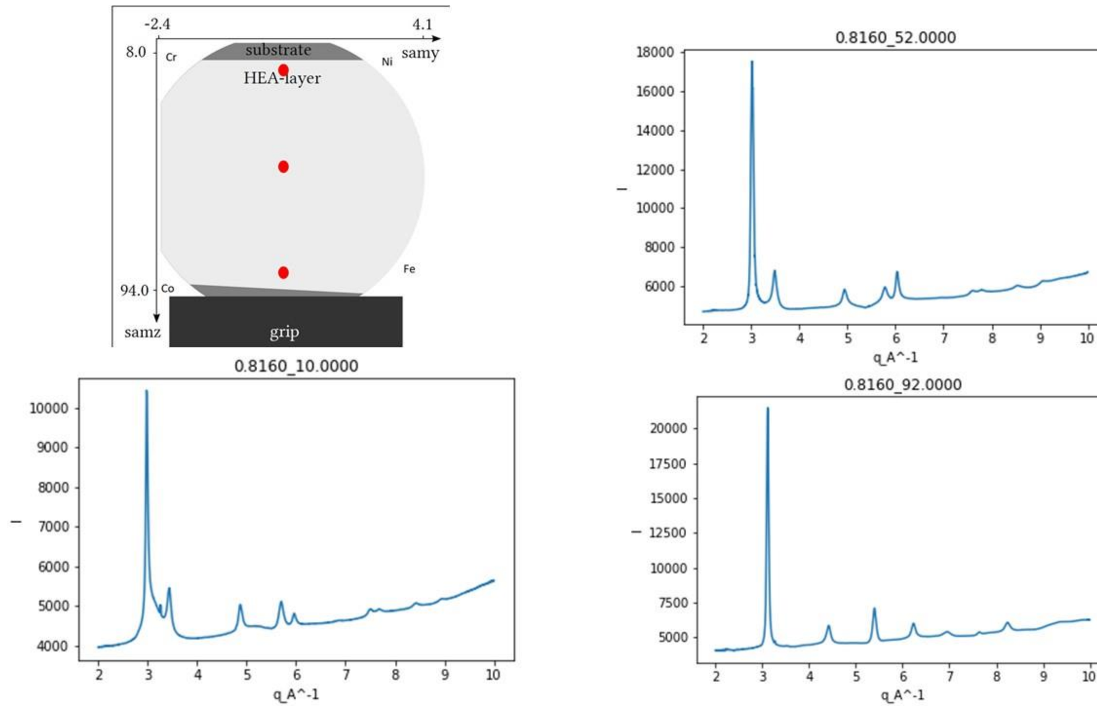

Figure 27. The three selected points in the wafer and the three diffractograms for these points.

The changes of the microstructure can be observed with changing the composition of the thin film. We can investigate the change of the crystallite size, the transition between phases and all the other properties of the microstructure of the thin film in a wide range of combination of the composition. The morphology and the mechanical properties of the sample will be investigated in the near future which will provide further possibilities to study the connection between the chemical composition, the microstructure and the mechanical properties.

Acknowledgment

First of all, I would like to thank my supervisors Jenő Gubicza and Pethö László for the professional advices and constant help for this work. I am very thankful for Empa - Swiss Federal Laboratories for Materials Science and Technology, for providing infrastructure during the research and Johanne Michler head of the Mechanics of Materials and Nanostructures group at Empa for providing the opportunity for me to join to the project. I want to say my thanks to Pascal Sortais and Gregoire Roussely for manufacturing the instrument, also I owe extra thanks to Gregoire for constantly upgrading the software of the instrument and providing tech support for me. I am most grateful for all the helps that I from Nadia Rohbeck in the indentation and János Lábár in the SEM.

References

[1] J.-W. Yeh, S.-K. Chen, S.-J. Lin, J.-Y. Gan, T.-S. Chin, T.-T. Shun, C.-H. Tsau, S.-Y. Chang, Nanostructured high-entropy alloys with multiple principal elements: Novel alloy design concepts and outcomes, Advanced Engineering Materials 6 (2004) 299-303 https://doi.org/10.1002/adem.200300567

[2] B. Cantor, I.T.H. Chang, P. Knight, A.J.B. Vincent, Microstructural development in equiatomic multicomponent alloys, Materials Science and Engineering A 375-377 (2004) 213-218. https://doi.org/10.1016/j.msea.2003.10.257

[3] Y. Zhang, T. T. Zuo, Z. Tang, M. C. Gao, K. A. Dahmen, P. K. Liaw, Z. P. Lu, Microstructures and properties of high-entropy alloys, Progress in Materials Science 61 (2014) 1-93. https://doi.org/10.1016/j.pmatsci.2013.10.001

[4] F. He, Z. Wang, S. Niu, Q. Wu, J. Li, J. Wang, C. T. Liu, Y. Dang, Strengthening the CoCrFeNiNb0.25 high entropy alloy by FCC precipitate, Journal of Alloys and Compounds 667 (2016) 53–57. https://doi.org/10.1016/J.JALLCOM.2016.01.153

[5] W.-R. Wang, W.–L. Wang, S.–C. Wang, Y.–C. Tsai, C.–H. Lai, J.–W. Yeh, Effects of Al addition on the microstructure and mechanical property of AlxCoCrFeNi high-entropy alloys, Intermetallics 26 (2012) 44–51. https://doi.org/10.1016/J.INTERMET.2012.03.005

[6] C. Wang, W. Ji, Z. Fu, Mechanical alloying and spark plasma sintering of CoCrFeNiMnAl high-entropy alloy, Advanced Powder Technology 25 (2014) 1334-1338. https://doi.org/10.1016/j.apt.2014.03.014

[7] R. Valiev, Nanostructuring of metals by severe plastic deformation for advanced properties, Nature Materials 3 (2004) 511-516. https://doi.org/10.1038/nmat1180

[8] A. Heczel, M. Kawasaki, J. L. Lábár, J. Jang, T. G. Langdon, J. Gubicza, Defect structure and hardness in nanocrystalline CoCrFeMnNi High-Entropy Alloy processed by High-Pressure Torsion, Journal of Alloys and Compounds 711 (2017) 143-154. https://doi.org/10.1016/j.jallcom.2017.03.352

[9] D. H. Lee, M. Y. Seok, Y. Zhao, I. C. Choi, J. He, Z. Lu, J. Y. Suh, U. Ramamurty, M. Kawasaki, T. G. Langdon, J. Jang, Spherical nanoindentation creep behavior of nanocrystalline and coarse-grained CoCrFeMnNi high-entropy alloys, Acta Mater. 109 (2016) 314-322. https://doi.org/10.1016/j.actamat.2016.02.049

[10] P. F. Yu, H. Cheng, L. J. Zhang, H. Zhang, Q. Jing, M. Z. Ma, P. K. Liaw, G. Liu, R. P. Liu, Effects of high pressure torsion on microstructures and properties of an Al0.1CoCrFeNi high-entropy alloy, Materials Science and Engineering A 655 (2016) 283-291. https://doi.org/10.1016/j.msea.2015.12.085

[11] A. Marshal, K. G. Pradeep, D. Music, L. Wang, O. Petracic, J. M. Schneider, 2019. Combinatorial evaluation of phase formation and magnetic properties of FeMnCoCrAl high entropy alloy thin film library. Scientific Reports 9, 7864.

[12] A. R. Ruffa, "Thermal potential, mechanical instability, and melting entropy," Physical Review B, vol. 25, no. 9, p. 5895, 1982.

[13] J. W. Yeh, "Recent progress in high-entropy alloys," Ann. Chim. Sci. des Mater., vol. 31, no. 6, pp. 633–648, 2006.

[14] M. C. Gao, J.-W. Yeh, P. K. Liaw, and Y. Zhang, High-Entropy Alloys: Fundamentals and Applications. 2016.

[15] S. Ranganathan, "Alloyed pleasures: Multimetallic cocktails," Current science, vol. 85, no. 5, pp. 1404–1406, 2003.

[16] Y. Zhang et al., “Microstructures and properties of high-entropy alloys,” Prog. Mater. Sci., vol. 61, no. October 2013, pp. 1–93, 2014.

[17] A. Takeuchi and A. Inoue, “Classification of Bulk Metallic Glasses by Atomic Size Difference, Heat of Mixing and Period of Constituent Elements and Its Application to Characterization of the Main Alloying Element,” Mater. Trans., vol. 46, no. 12, pp. 2817–2829, 2005.

[18] B. S. Murty, J. W. Yeh, and S. Ranganathan, High Entropy Alloys. Elsevier, 2014.

[19] Y. Zhang, Y. J. Zhou, J. P. Lin, G. L. Chen, and P. K. Liaw, “Solid-solution phase formation rules for multicomponent alloys,” Adv. Eng. Mater., vol. 10, no. 6, pp. 534–538, 2008.

[20] K. Y. Tsai, M. H. Tsai, and J. W. Yeh, “Sluggish diffusion in Co-Cr-Fe-Mn-Ni high-entropy alloys,” Acta Mater., vol. 61, no. 13, pp. 4887–4897, 2013.

[21] O. N. Senkov, G. B. Wilks, D. B. Miracle, C. P. Chuang, and P. K. Liaw, “Refractory high-entropy alloys,” Intermetallics, vol. 18, no. 9, pp. 1758–1765, 2010.

[22] M. H. Tsai and J. W. Yeh, “High-entropy alloys: A critical review,” Mater. Res. Lett., vol. 2, no. 3, pp. 107–123, 2014.

[23] L. Gao, W. Liao, H. Zhang, J. Surjadi, D. Sun, Y. Lu, 2017. Microstructure, Mechanical and Corrosion Behaviors of CoCrFeNiAl0.3 High Entropy Alloy (HEA) Films. Coatings 7, 156. https://doi.org/10.3390/coatings7100156

[24] V. M. Nadutov, A. V. Proshak, S. Y. Makarenko, V. Y. Panarin, M. Y. Svavil'Nyj, Creation and Mössbauer studies of high-entropy physical vapor deposition by cathode arc evaporation (PVD CAE) coating AlFeCoNiCuCr, Materialwissenschaft Und Werkstofftechnik 47 (2016) 272–277. https://doi.org/10.1002/mawe.201600489

[25] C. H. Tsau, Y. C. Yang, C. C. Lee, L. Y. Wu, H. J. Huang, The low electrical resistivity of the high-entropy alloy oxide thin films, Procedia Engineering 36 (2012) 246–252. https://doi.org/10.1016/j.proeng.2012.03.037

[26] U. Helmersson, M. Lattemann, J. Bohlmark, A. P. Ehiasarian, J. T. Gudmundsson, Ionized physical vapor deposition (IPVD): A review of technology and applications, Thin Solid Films 513 (2006) 1-24. https://doi.org/10.1016/j.tsf.2006.03.033

[27] D. M. Mattox, Handbook of Physical Vapor Deposition (PVD) Processing, William Andrew, New York, 1998. https://doi.org/10.1016/B978-081551422-0.50008-5

[28] T. Thuillier, L. Latrasse, J. Angot, J. Médard, T. Lamy, P. Sortais, 2010. Ultracompact/ultralow power electron cyclotron resonance ion source for multipurpose applications, Review of Scientific Instruments. 81, 02B314 https://doi.org/10.1063/1.3272878

[29] J. Gubicza, P.T. Hung, M. Kawasaki, J.-K. Han, Y. Zhao, Y. Xue, J.L. Lábár, Influence of severe plastic deformation on the microstructure and hardness of a CoCrFeNi high-entropy alloy: a comparison with CoCrFeNiMn, Materials Characterization 154 (2019) 304-314. https://doi.org/10.1016/j.matchar.2019.06.015

[30] http://archaeometry.missouri.edu/xrf_overview.html

[31]http://www.fischer-technology.com/fileadmin/documents/broc/EN/BROC_X-RAY_Product_Line_952-008_en.pdf

[32] Raja, P. M. V, & Barron, A. R. (1934). Physical methods in chemistry and nano science. Nature. https://doi.org/10.1002/jctb.5000533702

[33] K. Nagao and E. Kagami, "X-Ray Thin-Film Measurement Techniques VII. Pole Figure Measurement," Rigaku Journal, Vol. 27, No. 2, (2011)

[34] G. M. Pharr, W.C Oliver, An improved technique for determining hardness and elastic modulus using load and displacement sensing indentation experiments, Journal of Materials Research 7 (1992) 1564-1583. https://doi.org/10.1557/JMR.1992.1564

[35] J. Gubicza, X-ray line profile analysis in Materials Science, IGI-Global, Hershey, 2014

[36] B. Clausen, T. Lorentzen, T. Leffers, Self-consistent modelling of the plastic deformation of F.C.C. polycrstals and its implications for diffraction measurements of internal stresses, Acta Mater. 46 (1998) 3087-3098. https://doi.org/10.1016/S1359-6454(98)00014-7

[37]. L. Feng, Y.-Y. Ren, Y.-H. Zhang, S. Wang, L. Li, 2019. Direct Correlations among the Grain Size, Texture, and Indentation Behavior of Nanocrystalline Nickel Coatings. Metals 9, 188.

[38] F. Tian, L.K. Varga, J. Shen, L. Vitos, Calculating elastic constants in high-entropy alloys using the coherent potential approximation: current issues and errors, Comput. Mater. Sci. 111 (2016) 350–358. https://doi.org/10.1016/j.commatsci.2015.09.058

[39] W. Huo, H. Zhou, F. Fang, X. Hu, Z. Xie, J. Jiang, Strain-rate effect upon the tensile behavior of CoCrFeNi high-entropy alloys, Materials Science and Engineering A 689 (2017) 366–369. https://doi.org/10.1016/j.msea.2017.02.077

[40] P. Sathiyamoorthi, J. Basu, S. Kashyap, K. G. Pradeep, R. S. Kottada, Thermal stability and grain boundary strengthening in ultrafine-grained

CoCrFeNi high entropy alloy composite, Materials and Design 134 (2017) 426-433. https://doi.org/10.1016/j.matdes.2017.08.053
[41] Y. V. Milman, A. A. Golubenko, S. N. Dub, Indentation size effect in nanohardness, Acta Mater. 59 (2011) 7480-7487. https://doi.org/10.1016/j.actamat.2011.08.027

NYILATKOZAT

Név: Nagy Péter

ELTE Természettudományi Kar, szak: Anyagtudomány

NEPTUN azonosító: M07ILF

Diplomamunka címe:
Processing and characterization of a multibeam sputtered nanocrystalline CoCrFeNi high-entropy alloy thin film

A **diplomamunka** szerzőjeként fegyelmi felelősségem tudatában kijelentem, hogy a dolgozatom önálló szellemi alkotásom, abban a hivatkozások és idézések standard szabályait következetesen alkalmaztam, mások által írt részeket a megfelelő idézés nélkül nem használtam fel.

Budapest, 2020

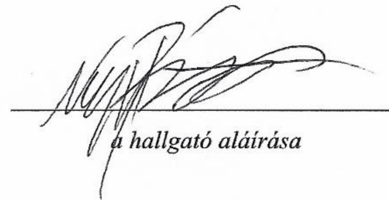

a hallgató aláírása